UNIVERSITY OF OKLAHOMA

GRADUATE COLLEGE

PORE-NETWORK MODELING AND ANALYSIS OF LABORATORY INDUCED HYDRAULIC FRACTURES

A DISSERTATION

SUBMITTED TO THE GRADUATE FACULTY

in partial fulfillment of the requirements for the

Degree of

DOCTOR OF PHILOSOPHY

By

ABHISHEK AGRAWAL
Norman, Oklahoma
2018

PORE-NETWORK MODELING AND ANALYSIS OF LABORATORY INDUCED HYDRAULIC FRACTURES

A DISSERTATION APPROVED FOR THE
MEWBOURNE SCHOOL OF PETROLEUM AND GEOLOGICAL ENGINEERING

BY

Dr. Deepak Devegowda, Chair

Dr. Ahmad Sakhaee-Pour, Co-Chair

Dr. Matthew Pranter

Dr. Mashhad Fahes

Dr. Zulfiquar Reza

Dr. Saeed Salehi

Acknowledgements

I would like to express my sincere gratitude to Dr.Ahmad Sakhaee-Pour for his continuous supervision of my research. He introduced me to the theoretical concepts of pore-network modeling and fracture mechanics which are the foundation of my Ph.D. research. Without his sustained guidance this research would not have been possible.

I would like to thank Dr.Deepak Devegowda for agreeing to serve as my advisor when Dr.Ahmad Sakhaee-Pour left for the University of Houston in the final phase of my Ph.D. program. Dr.Deepak Devegowda has since guided me on new research areas and provided feedback on the current work.

I would also like to thank my Committee members Dr.Matthew Pranter, Dr.Zulfiquar Reza, Dr.Saeed Salehi and Dr.Mashhad Fahes for critically reviewing my work and providing valuable comments for improving my dissertation.

Thanks to Mr.Akash Damani, Mr.Swetal Patel, Mr.Sayantan Ghosh, Mr.Davud Davudov, and Mr.Varahanaresh Sessetty for help with different aspects of my research.

I am grateful to Mewbourne School of Petroleum & Geological engineering for financially supporting my Ph.D. studies, and for providing the facilities and resources necessary to complete this work.

Finally, thanks to my family, friends, and colleagues for their support and encouragement through the duration of my studies.

Table of Contents

Acknowledgements iv

List of Tables viii

List of Figures ix

Abstract xiv

Chapter 1: Introduction 1

  1.1 Problem statement 1

  1.2 Objectives 4

  1.3 Hypotheses 5

  1.4 Summary of chapters 5

Chapter 2: Literature review 7

  2.1 Pore-scale modeling (Network modeling) 7

  2.2 Percolation approach 12

  2.3 Acoustic emission (relevance to percolation) 16

  2.4 Linear Elastic Fracture Mechanics (LEFM) 20

  2.5 Cycling loading 24

  2.6 Breakdown Pressure 26

  2.7 Limitations and Future Work 28

    2.7.1 Effect of thermal stresses 28

    2.7.2 Effect of injection rate and fluid viscosity 29

    2.7.3 Effect of reservoir fluid 29

    2.7.4 Effect of cyclic fracturing on casing failure 29

2.7.5 Effect of upscaling results from laboratory to field for cyclic fracturing.. 30

2.7.6 Effect of the accuracy of acoustic emission(AE) event locations 30

2.7.7 Carbonates 30

Chapter 3: Pore-scale modeling of acoustic emission (AE) events............................... 32

3.1 Constructing a network model using petrophysical measurements.................... 32

3.1.1 Mercury intrusion capillary pressures (MICP)... 32

3.1.2 Scanning Electron Microscopy (SEM) Images 34

3.1.3 Porosity... 34

3.1.4 Permeability... 35

3.2 A physically representative model of Tennessee sandstone.............................. 36

3.3 Hydraulic fracturing of a Tennessee sandstone block 39

3.4 Integrating acoustic emission into percolation theory to predict permeability enhancement 44

Chapter 4: Predicting permeability enhancement based on percolation theory 47

Chapter 5: Workflow for predicting breakdown pressure and breakdown cycle in cycling fracturing.. 54

5.1 Cyclic fracturing of the Tennessee sandstone sample 54

5.2 Methodology.. 59

Chapter 6: Predicting breakdown pressure and breakdown cycle in cycling fracturing 62

Chapter 7: Discussion and future works... 65

7.1 Pore-scale modeling of acoustic emission (AE) events 65

7.2 Cyclic fracturing 66

Chapter 8: Conclusions.. 68

8.1 Pore-scale modeling of AE events 68

8.2 Cyclic fracturing 69

References 71

Appendix 78

List of Tables

Table 1 – Spatial location, number of AE events, and the block volume of the core plug extracted from the stimulated Tennessee sandstone block shown in Figure 26. 49

Table 2 – Plug length, diameter, and permeability at 300 psi effective stress 49

Table 3 – Porosity and permeability of the Tennessee sandstone samples analyzed here. Lab measurements are based on the data available in the literature (Patel et al. 2017). 55

Table 4 – Breakdown pressures and number cycles of four Tennessee sandstone samples under triaxial loading conditions (vertical stress = 3000 psi, maximum horizontal stress = 2000 psi, minimum horizontal stress = 500 psi) 55

Table 5 – Fluid volume, breakdown pressure, and energy of different hydraulic fracturing methods. 66

List of Figures

Figure 1 – Oil production in the United States (2000 – 2015), million barrels per day (U.S. Energy Information Administration) 1

Figure 2 – Marketed natural gas production in the United States (2000-2015) billion cubic feet per day (U.S. Energy Information Administration) 2

Figure 3 – Schematic of a network modeling approach at pore scale. The black dots represent the pore sites and the blue lines denote the pore-throats. The pore space is represented by a square lattice (Sakhaee-Pour and Bryant, 2015) 7

Figure 4 – Bundle-of-tubes model used to simplify the pore structure of the rock. The tubes represent the void space. 8

Figure 5 – Sphere packing model, void space between spheres represent the flow path or pore space 9

Figure 6 – Two-dimensional network of tubes (regular lattice) proposed by Fatt (1956). 10

Figure 7 – Acyclic pore models. Narrower throats do not limit the access to the wider throats. (Sakhaee-Pour & Bryant, 2015) 11

Figure 8 – Scanning electron microscopy image of a tight-gas sandstone sample. (Sakhaee-Pour and Bryant, 2014) 11

Figure 9 – Percolation phenomenon is shown in the hexagonal lattice when there is a percolating path for the fluid to flow from one end to another, shown by a red line. The grey lines indicate the absence of a path for fluid to flow. 12

Figure 10 – A network of pores (sites) and pore-throats (bond) in a square lattice. 13

Figure 11 – Site percolation and bond percolation problems in 2D square lattice networks. The red lines indicate the presence of bond or site, while gray ones indicate the absence of bond/sites. The green lines show the clusters in the network................ 14

Figure 12 – A typical micro seismic event pattern. 17

Figure 13 – A elliptical crack under uniform tension, *a* is the major axis, *b* is the minor axis. (Fatemi, 2006)... 20

Figure 14 – The geometry of a straight, double-ended crack under uniformly applied stress. (Fischer-Cripps, A.C., 2007) 21

Figure 15 – Schematic of the three modes of crack surface displacement. (Farahmand, 2001)... 23

Figure 16 – Schematic of crack propagation with change in the stress intensity factor in cyclic loading (Paris et al. 1961). Paris' law (Eq. 3) is usually applied to the linear (middle) section of the plot.. 25

Figure 17 – Diagnostic Fracture injection test to determine the breakdown pressure. The red curve represents the pressure and the black curve represents the injection rate. (Barree et al, 2015) 28

Figure 18 – Mercury intrusion capillary pressure in drainage (1 to 4). The thickness of the lines denotes the throat size, and the red color indicates that mercury has already invaded in that throat. The corresponding change in wetting phase saturation with increasing saturation is shown in the lower graph. Note that (1), (2), (3) & (4) marked on the capillary pressure curve corresponds to the network model (1) through (4). (Sakhaee-Pour and Bryant, 2015).. 34

Figure 19 – An equivalent pore network representing a porous space P_{high} and P_{low} are the inlet and outlet pressures respectively. 36

Figure 20 – Tennessee sandstone core plug 36

Figure 21 – (a) Capillary pressure measurements of a Tennessee sandstone shows a plateau-like trend, which is consistent with a random pore-throat size distribution in the network of connected pores. (b) Pore-throat size distribution of the sample is determined based on the Young-Laplace relation. 37

Figure 22 – Hydraulic fracturing lab experimental setup. The figure on the left shows an expanded view of the triaxial loading system with axial loading, confining vessel and flat jacks to apply transverse stress. The figure on the right shows the sample covered with copper jacket mounted on the base plate of the triaxial loading system. (Damani et al., 2012; Damani, 2013). 41

Figure 23 – Pump pressure and cumulative AE events with time........ 42

Figure 24 – Spatial locations of 1564 AE events recorded during hydraulic fracturing of a Tennessee sandstone block in an (a) three-dimensional coordinate system, (b) X-Y plane, and (c) X-Z plane. (d) The size of the blue bubbles corresponds to the amplitude of the AE events. The green circles represent the sensor locations........ 43

Figure 25 – (a) Site percolation where the pore body (site) is filled randomly by the fluid. The black color corresponds to the absence of the fluid. (b) Shows a condition where percolation takes place, and there is a connected-through path from the left to the right of the model. (c) A conceptual model for pore-scale modeling of an AE event. The AE events are assumed to be indicators of micro-fractures that interact with the adjacent pore bodies of the intact pore space. 45

Figure 26 – (a-b) Block-scale sample of a hydraulically fractured Tennessee sandstone, where the holes show the locations of the extracted core plug for permeability measurements. The fracture left, and right wings are shown by blue, red lines, respectively. (c) Scanning electron microscope (SEM) image of the fractured core plugs that shows a connected-through fracture in the sample. 48

Figure 27 – The permeability decreases as the effective stress increases for different plugs. 51

Figure 28 – Core-scale measurements corroborate the physically representative pore model, which predicts the permeability enhancement based on percolation theory. The stimulated permeability remains very close to that of the matrix, as opposed to that of the fractured plug, when the number of AE events per unit volume (#AE/volume) is smaller than the percolation threshold. 52

Figure 29 – #Events/volume decreases monotonically with increasing amplitude cutoff 53

Figure 30 – Pump pressure data show that Samples 1 and 2, which were conventionally fractured, have higher breakdown pressures than do the cyclically fractured samples (3 and 4). The breakdown pressure of Sample 4 is higher than that of Sample 3 but requires fewer cycles to fail. 57

Figure 31 – The number of acoustic emission (AE) events is higher in cyclic fracturing (bottom) than in conventional fracturing (top), which suggests that the stimulated reservoir volume is larger in cyclic fracturing. The triaxial stresses were σ_v (vertical stress) = 3000 psi, σ_H (maximum horizontal stress) = 2000 psi, and σ_h (minimum horizontal stress) = 500 psi. 58

Figure 32 – Flowchart to determine the unknown parameters (C, m, and a_i) in the modified Paris' law (Eq. 9). The tuned model, whose accuracy is tested for Sample 4, helps us to predict the breakdown pressure and cycle. 61

Figure 33 – Error (Eq. 10) in predicting the breakdown pressure for cyclic fracturing for Sample 4. The unknown parameters in the modified Paris' law are determined based on the workflow provided in the Methodology for Sample 3. 63

Figure 34 – Predicted failure for two scenarios based on the tuned model: Case 1 shows a higher breakdown pressure at a lower number of cycles than does Case 2. 64

Abstract

Well stimulation is undertaken to reduce the restriction to flow in a reservoir. Among all the well stimulation techniques, hydraulic fracturing is one of the most widely employed techniques due to the development of shale and tight sand resources. The present study focuses on two problems relevant to hydraulic fracturing; predicting the transport properties enhancement as a function of recorded acoustic emission (AE) events during hydraulic fracturing and predicting the breakdown pressures in cyclic fracturing.

To study the first problem, I initiate pore-scale modeling of acoustic emission (AE) events based on percolation theory. The primary objective is to predict the permeability enhancement by accounting for the number of AE events. I first develop a physically representative model of the intact pore space of the matrix of Tennessee sandstone at the core scale based on petrophysical measurements, which are porosity, permeability, and capillary pressure. A block-scale sample of the formation is then hydraulically fractured, where piezoelectric sensors record the events generated during stimulation. I predict the permeability enhancement of the formation at the core scale by accounting for the number of AE events per unit volume. Independent petrophysical measurements corroborate the predicted results based on percolation theory. The proposed model has significant implications for characterizing the transport properties of the stimulated reservoir volume.

The second problem is relevant to predicting the breakdown pressure in hydraulic fracturing. In conventional fracturing, the fluid pressure is increased monotonically to reach failure in a single cycle. The breakdown pressure can be reduced if we increase and decrease the fluid pressure cyclically (cyclic fracturing). This phenomenon has been tested in other fields, but it is not yet possible to predict the breakdown pressure and cycle in petroleum engineering in the context of hydraulic fracturing. The present study proposes a workflow based on a modified Paris law to predict the breakdown pressure and cycle of cyclic fracturing. The modified Paris law is based on linear elastic fracture mechanics (LEFM), which treats the solid domain as an isotropic and linear elastic medium. I use the data available in the literature for dry Tennessee sandstones. The samples were hydraulically fractured under triaxial stress, two with conventional and two with cyclic methods. The results show that the tuned Paris law can predict the breakdown pressure and cycle with reasonable accuracy. The tuned model can help us to design an optimum scenario that is fundamentally different from the conventional method for formation stimulation.

Chapter 1: Introduction

1.1 Problem statement

In hydraulic fracturing, large volumes of fluid and sand are injected into the formation to enhance its transport properties. The technique has been used since 1940's but has gained momentum in this decade due to applications in unconventional resources like tight sandstones and shales. Hydraulic fracturing with a horizontal well is now one of the major methods of economically extracting oil and gas from low permeability reservoirs and accounts for about half of current U.S. crude oil production (Figure 1) and two-thirds of U.S. natural gas production (Figure 2)

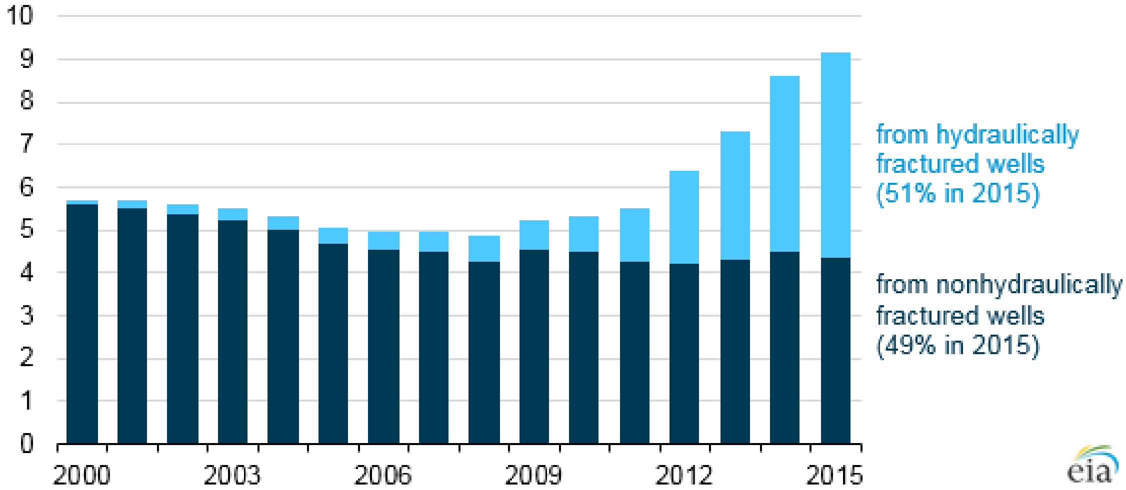

Figure 1 – Oil production in the United States (2000 – 2015), million barrels per day (U.S. Energy Information Administration)

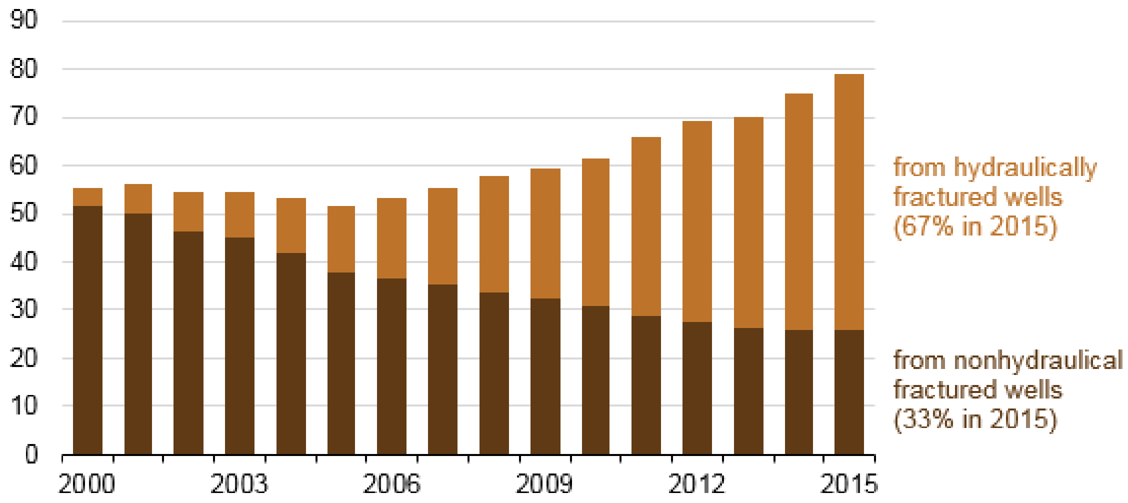

Figure 2 – Marketed natural gas production in the United States (2000-2015) billion cubic feet per day (U.S. Energy Information Administration)

Hydraulic fracturing has been successfully used in directional and vertical wells, both natural gas and oil wells. The technology of hydraulic fracturing is rapidly advancing but still not very well understood, and there is vast scope for improvement in both design and efficiency of the implementation.

For example, in hydraulic fracturing, fluids are injected into the formation at a sufficiently high rate that leads to the breakdown of the formation and creation of high conductive pathways for the reservoir fluid to flow toward the wellbore. Ideally, a single vertical fracture should be created with two wings that are 180 degrees apart and which are identical in shape and size. Bi-wing fractures are generated only if the rock is homogeneous and isotropic, but that is seldom the case in reservoirs. Instead, a complex network of fractures is created, so the geometry and orientation of the fracture become difficult to estimate. Estimating the permeability enhancement due to a simple bi-wing fracture is well documented in the literature (Prats, 1961). However, predicting the permeability enhancement due to a complex fracture network is not very well understood. A better approximation of the location and size of the connected fractures is crucial for evaluating the success of formation stimulation and for modeling reservoir performance. The fracture orientation is also critical for the stimulation of the reservoir efficiently with minimum interference. Acoustic emission events are used as a diagnostic tool to estimate the stimulated reservoir volume and are used for determining the fracture geometry an orientation. The first problem of the present study is that although acoustic emission events are helpful to understand post-fracture reservoir properties, predicting the transport properties enhancement as a function of recorded acoustic emission (AE) events is not well understood.

Cyclic fatigue of materials causes the material to fail below its static strength. There have been numerous studies to confirm that brittle rocks show this behavior. More recently, researchers (Erarslan et al., 2011; Mighani et al., 2014) have shown a reduction in tensile strength of the rock by cycling loading of Brazilian tests. Hulse (1959) used the concept of cyclic fatigue and applied it to hydraulic fracturing. He patented the pre and post-breakdown cyclic injection which improved the productivity compared to conventional hydraulic fracturing. In pre-breakdown cyclic injection, a series of pressure shocks are applied before reaching the breakdown pressure observed in conventional fracturing; this caused a weakening of the rock and a creation of multiple fractures. Similar results were observed in post-breakdown cyclic injection, in which the pressure shocks are applied after the breakdown pressure.

Zang et al. (2013) showed that there is an increase in formation permeability and reduction in seismicity by post-breakdown cyclic injection using simulations. Patel et al. (2017) conducted a series of laboratory cyclic fracturing experiments under triaxial loading and observed that the breakdown pressure of the rock decreases when fluid is injected in cycles. This method of fracturing is useful as less pump horsepower will be required to fracture the formation.

All the above studies show the benefits of cyclic fracturing over conventional fracturing, but none have developed a model to predict the breakdown pressures in the case of cyclic fracturing. Currently, the breakdown pressure for cyclic fracturing is estimated experimentally in the laboratory which is expensive and time-consuming.

1.2 Objectives

The present study is concerned with the formation stimulation of tight sandstones at the core and the block scales. The pore-scale modeling and the Linear elastic fracture mechanics are applied. The main objectives of the study are the following:

a) To predict the permeability enhancement of Tennessee sandstone via analyzing AE events. We develop a physically representative model for the pore space at the core scale, which embraces pore-throats and pore bodies. We then use the percolation theory to predict the permeability change at the core scale. The predicted results are tested against lab measurements.

b) To predict the number of pressure cycles and breakdown pressure during cyclic fracturing for Tennessee sandstone. Cyclic fracturing is a process in which the solid medium fails before reaching its ultimate strength. We assume that the Linear elastic fracture mechanics (LEFM) is valid and use the Paris law (Paris et al., 1961) which is an empirical equation to model cyclic fracturing and predict the number of pressure cycles required for the rock to fail and the breakdown pressure.

1.3 Hypotheses

Acoustic emission is recorded to assess the success the of the stimulation job. We assume that each acoustic emission (AE) event is a proxy for a microfracture created. The <u>first hypothesis</u> is that we can predict the permeability enhancement of a formation based on percolation theory if each event is considered as a proxy for microfracture. The microfractures will form a connected path when the number of events becomes larger than a specific value (threshold value).

The <u>second hypothesis</u> is that we predict the breakdown pressure and the number of cycles of a Tennessee sandstone based on the Paris Law under low-cycle loading. The Paris law is usually used for high-cycle loading, and its accuracy for low-cycle loading will be tested in the present study.

1.4 Summary of chapters

Chapter 2 review the basic concepts required for the conducted study. It includes pore-scale modeling, percolation theory, acoustic emission, Linear elastic fracture mechanics, and cyclic fracturing.

Chapter 3 discusses the construction of a pore network model of Tennessee sandstone. The general pore-network model is first reviewed. Then, it is shown how we can construct the model for Tennessee sandstone. It then explains the procedures for the laboratory hydraulic fracturing of the sample and the acoustic emission integration into the network model.

Chapter 4 covers the results of the permeability prediction based on the network model. It shows the number of acoustic emission (AE) events per unit volume for different tests.

Chapter 5 discusses the methodology that is used to predict the breakdown pressure in cycling fracturing. First, I illustrate how cyclic fracturing was conducted in the laboratory and show the laboratory results for the breakdown pressure and the AE events recorded. Then I present the workflow to predict the breakdown pressure and cycle.

Chapter 6 shows the results of predicting the breakdown pressure and the breakdown cycle based on the Paris law. The tuned model is also used for hypothetical cases with different paths for the cyclic loading. The hypothetical scenarios are crucial as they can provide a convenient tool for design an optimum scenario for formation stimulation.

Chapter 7 is a discussion of the work on both topics of pore-scale modeling of acoustic emission and cycling fracturing.

Chapter 8 presents the concluding remarks of the dissertation. It also provides suggestions for the extension of the conducted research in future.

Chapter 2: Literature review

2.1 Pore-scale modeling (Network modeling)

The topology of pore space controls the transport properties; hence, accounting for the interactions and distributions of pores-bodies in the rock is vital. Pore-scale modeling refers to the theoretical study and analysis of the rock structure at pore-scale to replicate its geometry and topology and capture the flow through the porous medium (Bryant, Mellor, & Cade, 1993).

In pore-scale modeling, we construct a physically representative model of the pore space. The pore space in the rocks is simplified to pore sites (pore bodies) and the pore-throats. The pore-throats are the narrow regions of the pore space, and the pore bodies are the wide parts (Figure 3). The narrow section dictates the resistance of the formation against the flow whereas the wide parts are relevant to its storage.

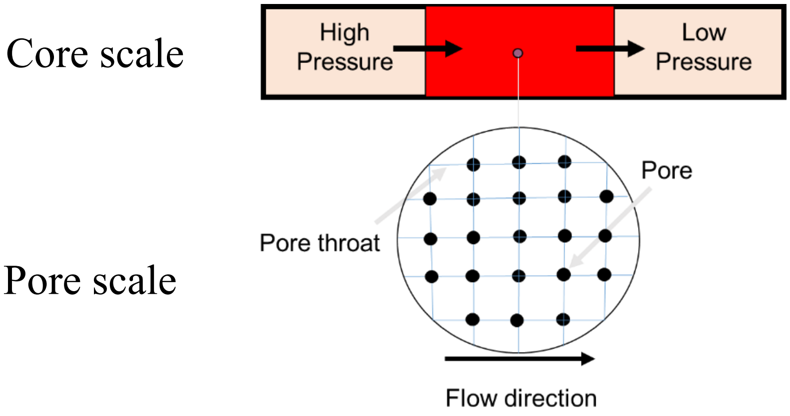

Figure 3 – Schematic of a network modeling approach at pore scale. The black dots represent the pore sites, and the blue lines denote the pore-throats. The pore space is represented by a square lattice (Sakhaee-Pour and Bryant, 2015)

There are two approaches to pore-scale modeling, theoretical and non-theoretical. Non-theoretical models are developed by extracting pore network directly from high-resolution images which means that it does not assume any pore distribution to develop the model. In theoretical models, we assume a distribution of pore-throats and pore bodies to develop the model and validate it with lab measurements (Sakhaee-Pour and Bryant, 2015). We do not review here studies that are based on non-theoretical models as extracting the pore space from images is out of scope of this work. We will discuss some of the theoretical models that include bundle of tubes, regular lattice, sphere packing, acyclic pore model, and multi-type model.

Washburn (1921) proposed the first theoretical pore models where he simplified the pore space to cylindrical capillaries. This concept was further extended by Purcell (1949) to predict the permeability from the bundle-of-tubes model using mercury intrusion capillary pressure measurements. The parallel capillary tubes in Purcell's model were circular in cross-section with different radii (Figure 4). Purcell (1949) was able to relate the permeability of a system to the porosity and capillary pressures.

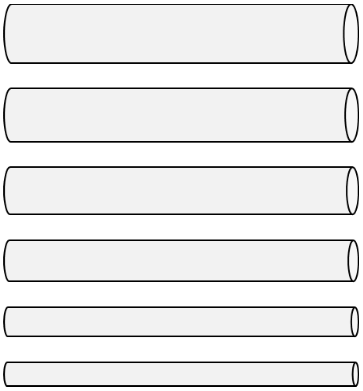

Figure 4 – Bundle-of-tubes model used to simplify the pore structure of the rock. The tubes represent the void space.

Later work by researchers on thin-section images of the rocks showed bundle of tubes was not an accurate representation of the pore space. Also, it could not capture the residual phases. Therefore, the sphere-packing model was developed (Fatt, 1956). In sphere pack models (Figure 5), the porous medium is said to consist of spheres representing the grains and the space between the spheres as void spaces through which fluid flows (Finney, 1970). The effects of grain sedimentation, compaction, and diagenesis on transport properties can be analyzed using this model. (Bryant, King, & Mellor, 1993)

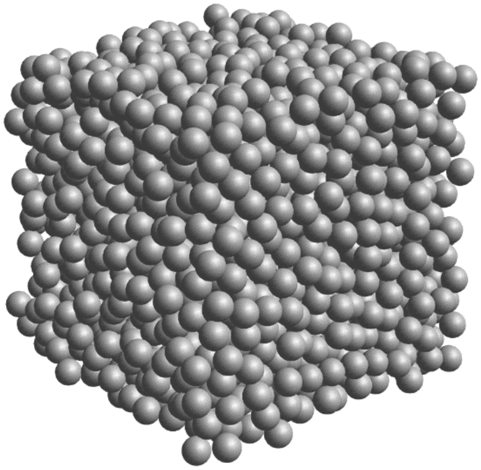

Figure 5 – Sphere packing model, void space between spheres represent the flow path or pore space

The advantage of this model, compared to the bundle of tubes, is that it provides a more accurate representation of the pore space, but it is more difficult to implement. Fatt (1956) introduced the notion of network of tubes as in a regular lattice. Lattice networks have a simple geometry, which eases the calculation of the transport property. Lattice network consists of a regular two-dimensional of tubes with randomly distributed sizes that represent the pore-throat size (Figure 6).

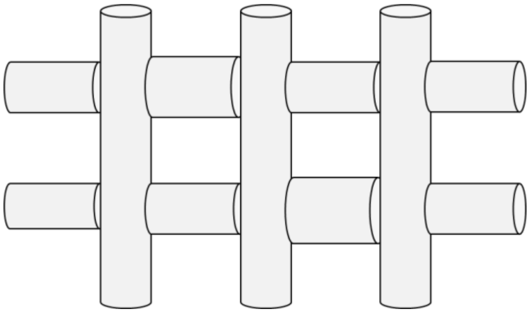

Figure 6 – Two-dimensional network of tubes (regular lattice) proposed by Fatt (1956).

The regular lattice and the sphere-packing models are called cyclic network models and are very popular. The notion of interconnectivity in these models allowed researchers to model two-phase permeability (Bryant et al., 1993), drainage (Mason and Mellor, 1995), and flow of non-Newtonian fluids (Balhoff and Thompson, 2004, 2006). It is now widely used for sandstones, but they fail to capture the transport phenomena or are not able to capture the variation of the capillary pressure with wetting phase saturations in tight gas sandstones (Mousavi and Bryant, 2012) and shales (Sakhaee-Pour & Bryant, 2015). Hence, the acyclic models, in which the distribution of pore bodies is such that there is only one path between any two pores, were developed by Sakhaee-Pour (2012). In acyclic models, the accessibility of wider pores is not restricted by narrower pores (Figure 7 – Acyclic pore models. Narrower throats do not limit the access to the wider throats. (Sakhaee-Pour & Bryant, 2015). An example of an acyclic model is a Bethe lattice (Bethe, 1935) which has a tree-like structure.

Figure 7 – Acyclic pore models. Narrower throats do not limit the access to the wider throats. (Sakhaee-Pour & Bryant, 2015)

In tight rocks, the pore space might be intergranular dominant, intermediate or intra-granular dominant. The intergranular dominant region is modeled with conventional network models, and the intra-granular space is modeled with tree-like pore structure (an acyclic network). The tree-like model (where the pore-throats distribution resembles a tree), each pore-throat is accessible through a wider pore-throat (no accessibility restrictions) shown in Figure 7. This combination of the two models is called as multi-type pore models (Sakhaee-Pour and Bryant, 2014) as shown in the figure below.

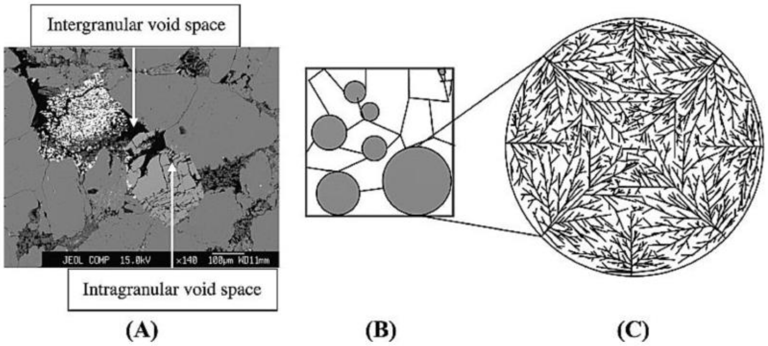

Figure 8 – Scanning electron microscopy image of a tight-gas sandstone sample. (Sakhaee-Pour and Bryant, 2014)

2.2 Percolation approach

There are many physical phenomena in which fluid spreads randomly through a medium. Solute diffusing through a solvent, molecules penetrating a porous solid, disease affecting a community (Broadbent and Hammersely, 1957). Percolation is concerned with a connected path that spans the domain randomly (Figure 9), the randomness can be due to the fluid, or due to the medium, it is traveling through. Diffusion is associated with randomness due to fluid while percolation is randomness due to the medium. Therefore, in percolation, fluid particles can be trapped, but it cannot be trapped in diffusion. (Barrufet & White, 1994). Percolation theory has been applied in many fields like petroleum engineering, hydrology, fractal mechanics and phase transitions (Berkowitz and Ewing, 1998).

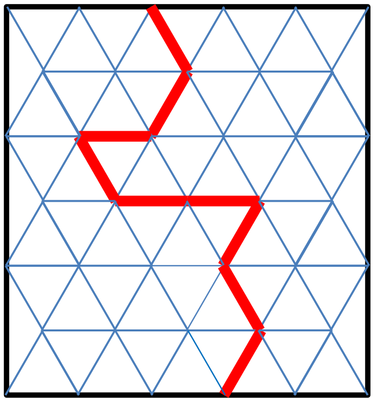

Figure 9 – Percolation phenomenon is shown in the hexagonal lattice when there is a percolating path for the fluid to flow from one end to another, shown by a red line. The grey lines indicate the absence of a path for fluid to flow.

The percolation theory is often applied using the network modeling approach to understand the transport properties in porous media. The network models are physically representative models of the pore space as they allow us to simulate different laboratory measurements. A regular two-dimensional network of pores (sites) that are connected by narrower throats (bonds) is an example of such shown in Figure 10.

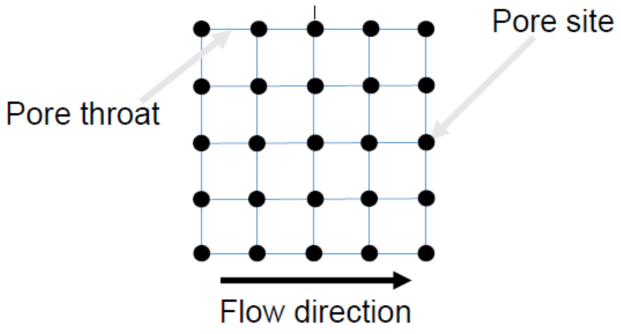

Figure 10 – A network of pores (sites) and pore-throats (bond) in a square lattice.

Each network is defined by a coordination number (*Z*), which is defined as the maximum number of bonds that can be connected to a pore site. In the above square network (Figure 10), the coordination number is four, and for a 3D cubic network, the coordination number is six (Behseresht, 2008). There is another basic term in percolation, the degree of connectivity. It is defined for a specific pore and is the ratio of the number of existing bonds connected to that pore to the coordination number of the pore. An average of these connectivity degrees over a network represent the probability of each bond being present and is denoted by *p*. The value of *p* ranges from zero to one, zero representing when all the pores are isolated and one representing when all the pores are connected to each other.

Percolation is often classified into two problems, site percolation, and bond percolation as shown in Figure 11. Let's imagine the pore space that has all the pores connected (p=1); then we start removing the sites from the network, the value of p decreases until the last spanning cluster throughout the network disappears, this is the site percolation threshold. So, for a network, when the *p*-value is greater than the site percolation threshold, there is at least one spanning cluster that exists through which fluid can flow across the two sides of the network.

Analogous to the site percolation, the bond percolation problem occurs when we start at a network where all the pores are connected (*p* = 1), and we begin to break the connection and decrease the p-value randomly*p*. The *p*-value reaches a threshold below which, there exists only isolated clusters, and there is no flow from one end of the network to the other. This phenomenon is known as bond percolation problem.

The threshold value can be determined analytically or by using Monte Carlo simulations, for different lattices and degrees (Dean and Bird, 1967). In the case of square lattice with degree four, the site threshold is 0.59, and the bond threshold is 0.5. Threshold values for other geometries can be found in Dean and Bird (1967). An example of the application of bond percolation is the decrease in porosity due to compaction and grain growth, where the pore-throats (bonds) eventually become entirely blocked (Bryant, Mellor and Cade, 1993).

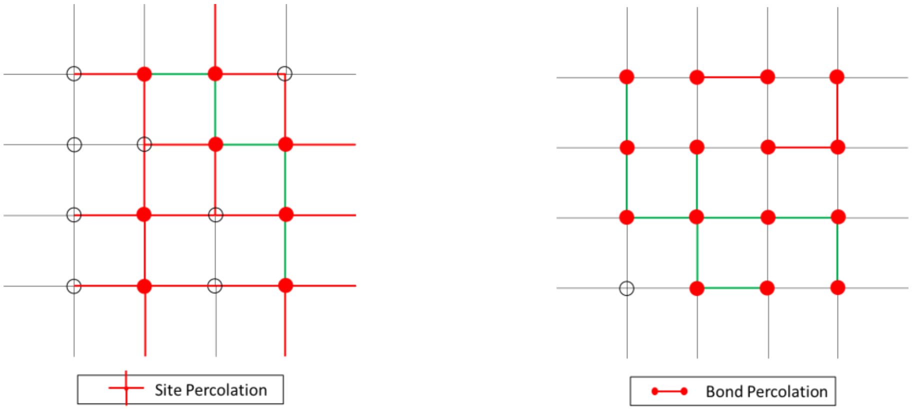

Figure 11 – Site percolation and bond percolation problems in 2D square lattice networks. The red lines indicate the presence of bond or site, while gray ones indicate the absence of bond/sites. The green lines show the clusters in the network.

Percolation theory sheds light on the larger scale behavior accounting for randomness in porous medium geometry, fluid properties and their interplay (Berkowitz and Ewing, 1998). Connectivity of the system elements essentially determines many properties of the macroscopic system. The properties of the system that emerge at the onset of macroscopic connectivity within it are known as percolation properties. Permeability is one such percolation property in porous medium which is determined by the connectivity of the elements in the system.

Network modeling can be used to describe the system which is a porous medium, and the elements are the sites and bonds in the system. Percolation processes are defined by accounting for the randomness. Hence, we distribute the pore-throat sizes randomly in our network model to demonstrate the percolation process.

We develop a network model to estimate the permeability enhancement based on the percolation theory by predicting the connectivity of the microfractures. We propose that until a specific threshold density of microfractures is reached, the microfractures do not percolate, and the formation permeability of the system remains low. The permeability increases significantly and becomes equal to the stimulated permeability when the small fractures become connected. The permeability variation is quantified in this study.

2.3 Acoustic emission (relevance to percolation)

An acoustic emission (AE) is a transient elastic wave generated by the rapid release of energy within a material (Lockner, 1993), which can be detected using seismometers. AE events are associated with brittle fractures due to pressure and temperature. Analyzing AE has applications in earthquake seismology (Lei and Ma, 2014), predicting rock bursts and mine failures, fracture mapping (Phillips et al., 1998), monitoring mechanical performance (Chong et al., 2003), and monitoring the condition of tools and health monitoring (Yapar et al., 2015).

AE takes different forms because of variations in the frequency and amplitude of waves. Both seismic and microseismic events – a physical concept in earthquake seismology – are derived from AE. The science of seismology's study of earthquake activity and the geophysical study of microseismic activity in rock are similar. There is a generation of acoustic signals whenever irreversible damage occurs (Lockner, 1993). The acoustic signals provide information about the size, the location, and the deformation mechanisms.

During Hydraulic fracturing, the rock breaks and energy is released in the form of elastic waves, compression (P) waves and shear(S) waves. Using a velocity model and travel time of the waves to the sensors, hypocenters of these acoustic emission events can be determined. The spatial distribution of hypocenters (Figure 12) gives information about fracture geometry, orientation and stimulated reservoir volume (SRV).

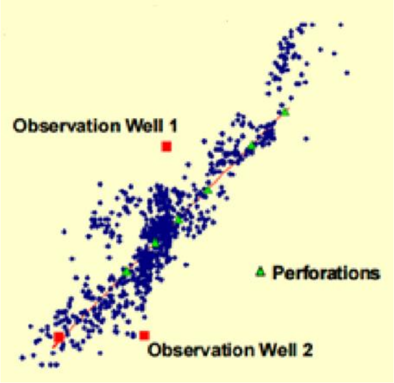

Figure 12 – A typical micro seismic event pattern. (Warpinski, 2010)

Indirect information about fracture mechanics like fracture complexity, stage effectiveness, and fluid movement can be obtained from analysis of AE events (Warpinski, 2010).

Microseismic monitoring is used as a diagnostic tool to evaluate the hydraulic fracture job. Microseismic is acoustic emission, AE, which are generated when rock deformation occurs due to fluid injection and energy is released in the form of waves which are captured by sensors. AE events, due to microcracks growth, precede the macroscopic failure of rock and concrete samples under constant stress or constant strain rate loading (Stein et al., 2003; Ge, 2003). Microseismic events are used as a proxy for the microcracks created during the fracturing process. There are a lot of publications like (Maxwell, 2010; Eisner et al., 2009) that show the use of microseismic events for understanding hydraulic fracture position, size, and orientation.

Then there are other researchers (Shapiro et al., 2002, 2005; Grechka et al., 2010) that indicate a possibility to estimate the permeability based on microseismic data. They assume that microseismic events are triggered by pore pressure increase per pressure diffusion equation. This is only useful in conventional reservoirs with higher permeability. In this case, microseismic events are created due to shear slippages related to fluid leak-off pore pressure changes caused by rapidly moving pressure transients in these high permeability reservoirs.

In tight sandstone and shale reservoirs, diffusivity-related pore pressure changes cannot move very far from the actual fracture planes, that implies that the three-dimensional microseismic cloud imaged in these reservoirs are equivalent to the actual fracture-network size and is termed as stimulated reservoir volume (SRV). Researchers have used the stimulated rock volume (SRV) for estimating well performance (Mayerhofer et al., 2010). SRV is a concept to illustrate the reservoir volume affected by the stimulation. It is important to note that it does not provide any means to identify the connectivity within the volume, that is the effective producing fracture structure.

Samil et al. (2014) showed an analytical method to calculate the fracture permeability at laboratory scale utilizing pressure data and acoustic emission location. But this method does not estimate the enhanced permeability of the region beyond the fracture. Researchers have also used a Kalman filter to interpolate the transport properties at the reservoir scale (Tarrahi et al., 2015).

A recent study has proposed using microseismic density to compute the effective producing SRV at the reservoir scale (Meek et al., 2015), where grid blocks with no events are unstimulated and have intact transport properties. The transport properties of grid blocks with AE events are increased using an ad-hoc model that is based on permeability obtained from diagnostic plots run on initial production data.

Researchers have analyzed the fracture propagation based on percolation theory. Under certain conditions, Scholz (1968) contented, the accumulation of damage and growth of cracks are random, - for example, in a natural rock, where heterogeneities are broadly distributed, and a statistical model can describe the variation of stress within the medium. Chelidze (1982) suggested that the initial stages of brittle fractures and percolation processes in a lattice are similar. He stated that multiple ruptures develop in solids, first single isolated microcracks appear, and then with the increase of load with time, the density of cracks increases, and they merge, and when a 'critical density of cracks' is attained, the main fracture is formed. He pointed the similarity of this physical phenomena with the percolation theory, where 'critical crack density' was equivalent to percolation threshold of a fracture with an infinite cluster.

Later, Sahimi (2003) suggested that percolation is a static process in which failure has nothing to do with the stress and strain field in the lattice, whereas the growth of fractures is not random, and depends on the stresses and strain in the solid. He also stated that, in the initial stages, the bonds that break are random, and the stress enhancement at the tip of a given microcrack is not large enough to ensure that the next microcrack occurs at the tip of the first microcrack. As more microcracks nucleate, the effect of stress enhancement becomes stronger, and deviations from random percolation increases.

The proposed models have had some success in predicting the production rate of a formation, but they have not been tested against core- or block scale measurements. The validity of the proposed models is critical, considering that reservoirs are highly heterogeneous, and different physics controls the effective transport properties at different scales.

2.4 Linear Elastic Fracture Mechanics (LEFM)

Hydraulic fracturing has become an essential part of the petroleum industry, as it enables us to produce hydrocarbon from tight formations by improving their transport properties. Multistage hydraulic fracturing is done in horizontal wells these days, which has dramatically increased the cost of completions and so it is necessary to optimize the fracturing process to lower the cost. Understanding and predicting the fracture geometry and orientation using fracture modeling before actual fracture job are essential for this purpose. Most of the existing techniques for fracture propagation modeling are based on linear elastic fracture mechanics (LEFM); thus, its relevant concepts are reviewed here.

Inglis (1913) started the linear elastic fracture mechanics (LEFM) by analyzing the stress field around an elliptical crack in brittle materials. He proposed that the stress at the crack tip is proportional to the length of the major axis of the crack and the tensile load (Figure 13).

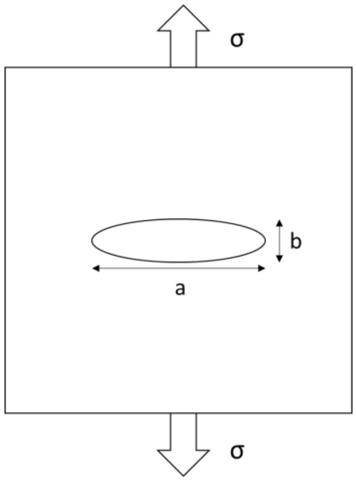

Figure 13 – A elliptical crack under uniform tension, *a* is the major axis, *b* is the minor axis. (Fatemi, 2006)

$$\sigma_A = \left(1 + 2\,\frac{a}{b} \right) \sigma = K_t \sigma \tag{1}$$

where a is the length of mthe ajor axis, b is the length of mithe nor axis, K_t is the stress concentration factor.

The stress concentration factor does not depend on the absolute size or the length of the hole but only on the ratio of the major and the minor axes (eq. 1). This was contrary to the fact that larger cracks are propagated more easily than smaller ones. This led Griffith (1920) to use the energy balance criterion to derive the relation for crack propagation and stated that for a crack extension, the amount of strain energy released must be greater than or equal to that required for the surface energy of the two new crack faces (Figure 14).

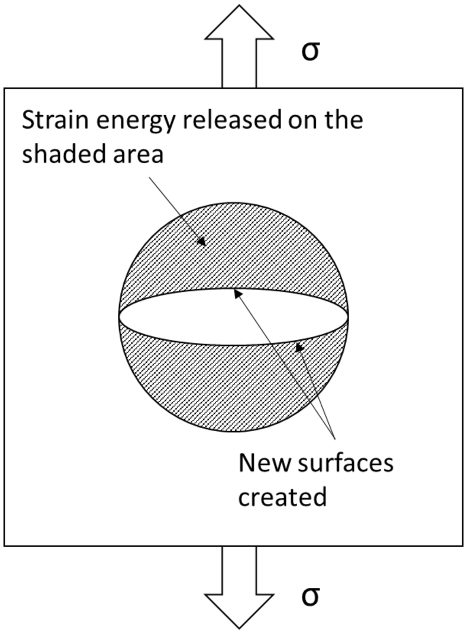

Figure 14 – The geometry of a straight, double-ended crack under uniformly applied stress. (Fischer-Cripps, A.C., 2007)

Three decades later, Irwin (1957) while working on the fracture of steel armor plating during penetration by ammunition described the stress at the crack tip in terms of the stress intensity factor (SIF). The stress intensity factor was a single parameter that could characterize the point of failure and was able to provide a quantitative method for dealing with both stresses and defect size. This approach assumes that the fracture initiates in the test specimen because a critical value of the stress and strain field has been reached.

In linear elastic fracture mechanics (LEFM), we assume that the solid medium is isotropic and linearly elastic (Stephens et al. 2000). LEFM has many applications because it simplifies the complex behavior of the solid medium. It also provides a reliable solution when the rock behavior is brittle. With these assumptions, the stress intensity factor (eq. 2) can be used to estimate the stress state near the crack tip as follows (Sakhaee-Pour et al. 2010):

$$K = Y\sigma_e\sqrt{\pi a} \quad \sigma_e = P_p - \sigma_c \tag{2}$$

Where K is the stress intensity factor, a is the crack length, Y is the geometric shape factor, σ_e is the effective pressure, P_p is the fluid pressure, and $\sigma_c$is the confining stress.

The stress intensity factor is like a “scale factor” for a particular crack system. In Eq 2, Y and π are constants, so the stress intensity K factor is equivalent to the stress magnitude at a position. K is proportional to the external stress applied σ_e, and the square root of the crack length a. That means doubling the externally applied stress will double the stress near a location at the crack tip and increasing the crack length four times for a given external stress will double the stress applied near the crack tip.

The stress intensity factor has three modes. The first mode is tensile, or opening, where the two crack surfaces move directly away from each other. The second mode is in-plane shear, or sliding, which occurs when the two crack surfaces move parallel to each other. The third mode is out-of-plane shear or tearing, which takes place when the crack surfaces slide over each other parallel to the leading edge (Figure 155). K_I, K_{II}, and K_{III}denote the SIFs of the first, second, and third modesK_I, K_{II}, and K_{III} respectively (Farahmand, 2001). The first mode is most relevant to our study, considering the loading conditions and the fracture geometry after the test.

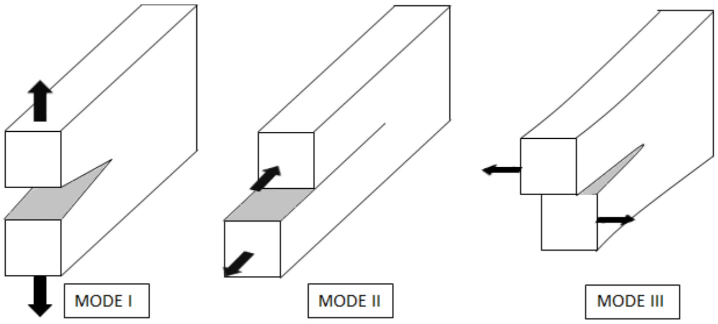

Figure 15 – Schematic of the three modes of crack surface displacement. (Farahmand, 2001)

The fracture toughness governs rock failure due to the presence of a crack. The sample fails when the effective stress intensity factor reaches the fracture toughness (K_{IC}), which is a medium property and does not depend on the loading conditions (Farahmand, 2001). The effective stress intensity factor reduces to K_I when only the first mode is active. For a given crack system, with an initial crack length, increasing the externally applied stress will cause K_I to increase and eventually become equal to K_{IC} resulting in fracture propagation.

2.5 Cycling loading

Cyclic loading, or fatigue (Shigley et al. 2004), is the application of fluctuating stresses or strains. It has many applications in other engineering fields, such as mechanical and aerospace engineering, examples of which include automobile axles, wheels, cranes, and various aircraft parts. The cyclic loading is often classified into high and low cycles. High-cycle failure (HCF) is a cyclic loading where the sample has a relatively long life (10^4- 10^8 cycles). Low-cycle fatigue, on the other hand, corresponds to large loading with a short life (< 10^4 cycles).

The life of a specimen under cyclic loading is often predicted using various versions of Paris law (Paris et al., 1961), which is an empirical correlation that predicts the crack growth in cyclic loading. It allows us to determine the residual life of a sample when its crack size is known. It predicts the crack growth, when the LEFM assumptions are valid, as follows (Paris et al. 1961):

$$\frac{da}{dN} = C\Delta K^m \qquad (3)$$

Where a is the crack length, N is the number of cycles, ΔK is the change in the stress intensity factor at each cycle, and C and m are constants (tuning parameters). The unknown parameters (C and m), which are the solid medium properties, are determined by fitting the empirical relation to the lab measurement (Figure 166).

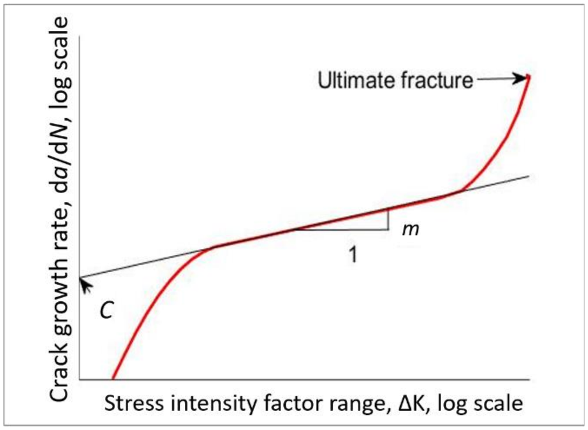

Figure 16 – Schematic of crack propagation with a change in the stress intensity factor in cyclic loading (Paris et al. 1961). Paris' law (Eq. 3) is usually applied to the linear (middle) section of the plot.

Paris's law is a powerful and simple tool. Paris original law (1961) has been improved over the years (Forman et al. 1967; Erdogan and Ratwani 1970; Elber 1971; Donahue et al. 1972). There are more advanced models that predict crack growth but require additional lab measurements (Farahmand, 2001), which may not be available. Thus, Paris' law is commonly used in fracture mechanics, even if its results may remain less accurate than the more advanced models.

In petroleum engineering, we usually increase the fluid pressure monotonically until the formation or rock sample fails, in conventional fracturing (a single cycle). In cycling fracturing, the fluid pressure is increased and decreased cyclically until the sample fails. This method differs from conventional fracturing, in which the fluid pressure is increased monotonically to reach failure in a single cycle.

The fracture toughness governs rock failure due to the presence of a crack. The rock fails at lower tensile stress in cyclic fracturing than in conventional fracturing due to the crack growth in the cycles (Patel et al., 2017). A larger crack length corresponds to a higher SIF for a given stress condition (Eq. 2).

In the present study, we model rock failure under cyclic loading based on a modified Paris law. We first determine the unknown parameters of the model based on those available in the literature. We then predict the breakdown pressure and the number of cycles required for another sample using tuned model. To do this, we propose a workflow, whose results are promising.

2.6 Breakdown Pressure

Haimson and Fairhurst (1969) performed hydraulic fracturing experiments on hydrostone to investigate the effects of borehole diameter and injection rate on breakdown pressure. Their study concluded that with increasing pressurization rate, breakdown pressure increases. They also found that the larger the borehole, the lower is the value of breakdown pressure.

Guo et al. (1993a, b) conducted fracturing experiments on gypstone blocks to study the effect of least principal stress on fracture propagation. They concluded that the breakdown pressure increased with increasing injection rate and vice versa.

Morita et al. (1996) performed hydraulic fracturing experiments on cubic blocks of Berea sandstone, Mancos shale, and Castlegate sandstone. They concluded that the breakdown pressure could not be predicted with existing theories, but it was thought to be a function of Young's modulus of the formation, wellbore size, and drilling fluid.

Bohloli and de Pater (2006) performed hydraulic fracturing experiments on saturated cylindrical rock samples of size 0.51m in length and 0.4m in diameter, prepared in the lab by compacting quartz sand of 90 µm grain size. They observed that the breakdown pressure was 1.5 to 2.5 times the minimum confining stress.

Jin et al. (2013) predicted breakdown pressures using a weight function method. They conducted sensitivity studies to investigate the influence of crack length, orientation, in-situ stress contrast and fracture toughness on breakdown pressure. Their results indicated that breakdown pressure decreases with increasing crack length. Crack orientation also influences breakdown pressure. There is the influence of stress contrast on breakdown pressure. As stress contrast increases, the breakdown pressure decreases (mostly effects smaller cracks). The breakdown pressure increases with increase in fracture toughness. The fracture toughness itself changes with rock type. Increasing confining pressure or temperature will increase the fracture toughness.

Breakdown pressure in the field can be obtained from a Diagnostic fracture injection test analysis (Barree et al., 2015). In a DFIT (Figure 17), the wellbore is filled up with fluid, and the fluid is continued to be injected causing the pressure to rise quickly until initial breakdown occurs. There will be a sharp drop in pressure when the breakdown occurs. Then fluids are continued to be pumped for more time to get the fracture to extend just outside the invaded zone and into the native reservoir. Next, the pump is shut which causes an instantaneous drop in pressure and the pressure recording at this instant is ISIP (Initial shut-in pressure). As we continue to monitor the shun in pressure, the fluid from the fracture leaks off into the formation. We are then able to determine the fracture closure pressure from the pressure fall off.

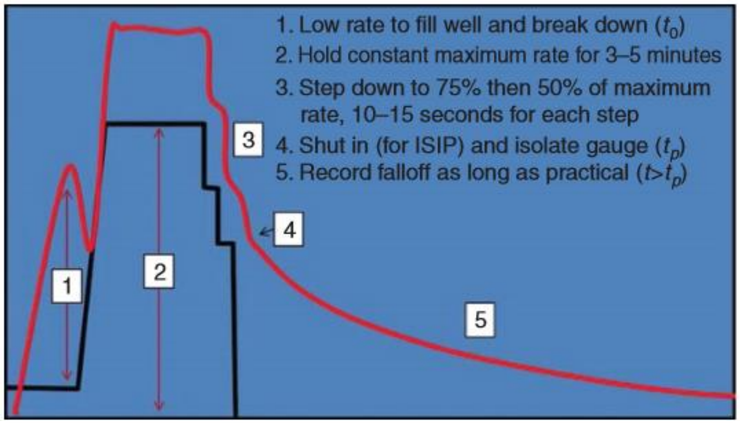

Figure 17 – Diagnostic Fracture injection test to determine the breakdown pressure. The red curve represents the pressure, and the black curve represents the injection rate. (Barree et al., 2015)

2.7 Limitations and Future Work

In our work, we study the breakdown pressure at laboratory scale with fixed confining pressure, room temperature, fixed stress anisotropy, homogeneous isotropic rock with 50 cp vegetable oil injection. Changing any of these variables may influence the results. Additional laboratory experiments to see these sensitivities are out of scope for this work. But for completeness, I discuss these sensitivities published in literature.

2.7.1 Effect of thermal stresses

In thermal fracturing technique, the temperature of rock in the near-wellbore zone is reduced. This is accomplished by injecting cold fluids into the hot reservoir rock which leads to the development of thermal fractures. Enayatpour et al. (2014) conducted discrete element method (DEM) analysis to study thermal fracturing in tight hydrocarbon formation. Their results showed that thermal fracturing enhances the permeability of rock through reduction of the effective stress and lowering of the tensile strength of the rock. Lowering the tensile strength results in a reduction in breakdown pressure.

2.7.2 Effect of injection rate and fluid viscosity

Jung et al. (2014) ran laboratory hydraulic fracturing experiments to see the influence of injection rate and viscosity on fracturing. They noticed that high viscosity and injection rate resulted in higher breakdown pressure because of the effect of fluid infiltration. They explained that the low viscosity fluid could easily penetrate around the borehole, causing the pore pressure to increase which reduce the effective stress around the borehole.

2.7.3 Effect of reservoir fluid

Warpinski et al. (2001) report field observations where they see a narrower microseismic cloud with respect to fracture length in a gas reservoir while they see a wider cloud with respect to fracture length in a liquid saturated reservoir.

2.7.4 Effect of cyclic fracturing on casing failure

Adams et al. (2017) show case histories where casing failure has occurred due to fatigue during hydraulic fracturing. They mention that fatigue failure may occur after a few cycles or after a lot more cycles and this kind of failure is not well understood. They point out that fatigue life is strongly influenced by the surface finish, residual stress, subsurface cracks, stress concentrations, chemical environment and the material toughness.

2.7.5 Effect of upscaling results from laboratory to field for cyclic fracturing

Zang, Stephansson & Zimmermann (2017) illustrated that the reduction in breakdown pressures observed in laboratory scale are also applicable in field scale. But they suggest that upscaling of cyclic hydraulic fracturing to wellbore scale should be approached with careful design of operational injection parameters like number of cycles, injection duration, interval duration, rate increment per cycle, number of fracturing stages, etc.

2.7.6 Effect of the accuracy of acoustic emission(AE) event locations

Moreno et al. (2011) conducted a laboratory hydraulic fracturing under uniaxial stress and recorded acoustic emission. They use microseismic event locations to measure the fracture dimensions. They note that hypocenter location accuracy affects the resolution of these dimensions. The accuracy of the event locations is affected by the velocity model and arrival time picking (Chitrala et al., 2010)

2.7.7 Carbonates

Carbonates are heterogeneous rocks which display triple porosity (pore-vug-fracture) and are mixed-to-oil-wet (Al-dhahli et al., 2011). Pore-network modeling has been carried out in carbonates by researchers (Kamath et al., 1996; Al-dhahli et al., 2011) to study the improved oil recovery. Carbonates with low permeability are stimulated using acid fracturing or slick-water fracturing with proppant depending on the conditions (Jeon et al., 2016). Recent studies have utilized microseismic monitoring to understand the stimulation results in carbonates at the field scale (Basu et al., 2014).

But still microseismic in carbonates is not very well understood and there is lack of published literature on the same. Pore-network modeling of hydraulic fracturing in carbonates is not attempted previously as far as we know. It could be a topic of future research.

Chapter 3: Pore-scale modeling of acoustic emission (AE) events

3.1 Constructing a network model using petrophysical measurements

A physically representative model of the pore space implies representing the pore bodies and pore-throats in a geometrical sense which enable us to capture the physics of flow through porous space. Some examples of physically representative models of pore space are a bundle of tubes, sphere models, and lattice network models.

To construct any such theoretical model of the intact pore space and validate it, we need petrophysical measurements. The most common petrophysical measurements required are capillary pressure curves, thin-section images, porosity, and permeability.

3.1.1 Mercury intrusion capillary pressures (MICP)

MICP allows us to determine the pore-throat size distribution of a rock sample. In mercury intrusion, we inject mercury in the sample by increasing the capillary pressure in small increments. The volume of mercury injected into the sample at every capillary pressure is recorded. Then using the Young-Laplace equation (Eq. 4), we convert the capillary pressure data to pore-throat size (Melrose, 1998).

$$P_c = \frac{2\sigma\cos(\theta)}{r} \tag{4}$$

where P_c is the capillary pressure, σ is the interfacial tension, θ is the contact angle, and r is the pore-throat radius. The injected volume at each capillary pressure gives the frequency of the pore-throat size distribution.

Figure 188 shows the change in saturation of wetting phase when the capillary pressure is increased. It shows that there are two possible trends for the curve, a plateau-like trend and a non-plateau like trend. When the capillary pressure is increased in steps, only pore bodies that are accessible to the mercury whose characteristic sizes are larger than the corresponding size of the capillary pressure are invaded.

Let us consider the pore network shown in Figure 188(1) – (4): as the capillary pressure is increased, we notice mercury fills up most of the pore space going from (2) – (3), this results in a plateau-like trend depicted in Figure 188 lower graph indicated by (2), (3) on the curve. This phenomenon occurs when there is a random pore-throat size distribution in the network. On the other hand, as indicated by the straight curve in the lower graph of Figure 188, the non-plateau-like trend is due to a uniformly increasing or decreasing pore-throat size distribution. This non-plateau-like trend occurs in shale and tight rocks and is modeled using tree-like network structure (Figure 7) with decreasing pore-throat sizes from the fluid entry point.

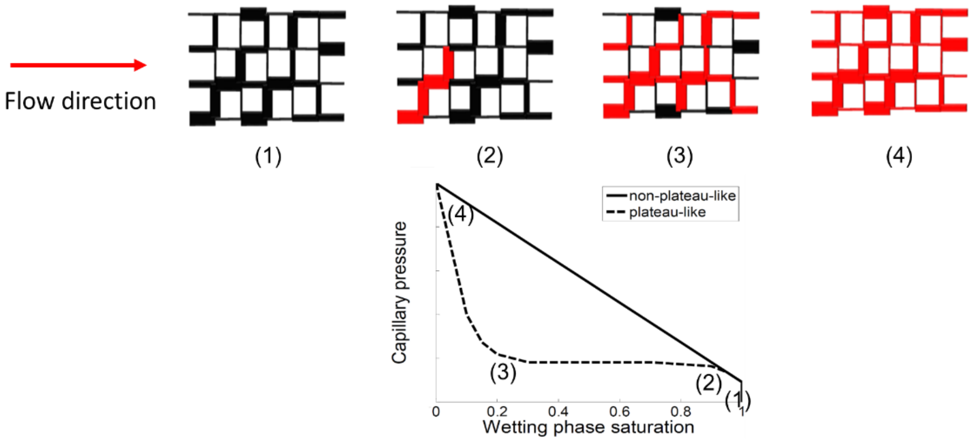

Figure 18 – Mercury intrusion capillary pressure in drainage (1 to 4). The thickness of the lines denotes the throat size, and the red color indicates that mercury has already invaded in that throat. The corresponding change in wetting phase saturation with increasing saturation is shown in the lower graph. Note that (1), (2), (3) & (4) marked on the capillary pressure curve corresponds to the network model (1) through (4). (Sakhaee-Pour and Bryant, 2015).

3.1.2 Scanning Electron Microscopy (SEM) Images

Constructing a network model requires assigning each cylindrical capillary tube a radius and a length. The radius is obtained from the MICP measurements, and the length is obtained from the average grain size extracted from the SEM images of the rock sample.

3.1.3 Porosity

Porosity is used to calculate the volume of hydrocarbons that can be stored in the rock. In network models, we create a network of tubes that occupy a given volume. The pore volume of our system is the sum of the volumes of the tubes that make up the network, which we can calculate, given the length and radius of the tube. The bulk volume is the size of the theoretical pore network times the thickness. We assume that the thickness is equal to the average of the pore-throat sizes. The network porosity is defined as a ratio of pore volume over bulk volume (eq. 5). To validate the network model, we match this calculated network porosity to the measured lab porosity of the intact sample. Network thickness is one of the adjustable parameters to match the lab results of porosity and permeability.

$$Network\ Porosity = \frac{Pore\ Volume}{Bulk\ Volume} \tag{5}$$

3.1.4 Permeability

The aim of creating a physically representative network model is to predict the transport properties of the rock. One such important transport property is the permeability. To obtain the permeability of the model, we apply a pressure difference across our network model, assuming steady state. Using the principle of conservation of flux, we calculate the pressure at every node and flux in every bond. This enables us to calculate the total flow passing through the network (Figure 199). Applying Darcy's law on the network, given the total flux and network dimensions, we obtain the effective permeability.

The pore-throat size, which is based on mercury injection capillary pressure measurements, is randomly distributed in the network of connected pores. The predicted permeability is then tested against independent lab measurements to test the model.

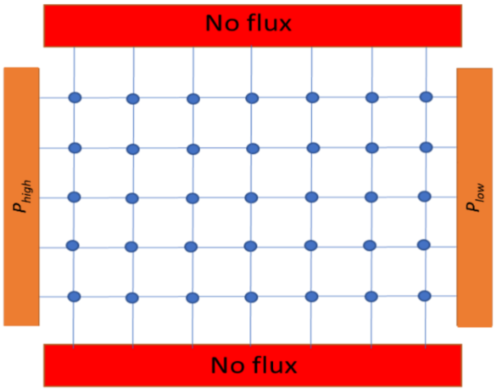

Figure 19 – An equivalent pore network representing a porous space P_{high} and P_{low} are the inlet and outlet pressures respectively.

3.2 A physically representative model of Tennessee sandstone

We analyzed Tennessee sandstone, which is homogeneous and light brown (Figure 20).

Figure 20 – Tennessee sandstone core plug (Reproduced from Damani, 2013)

Routine core analysis showed that the porosity and the permeability of an intact Tennessee core plug were equal to 5.5 % and 4 µd. Mineralogy was determined using Fourier Transform Infrared Spectroscopy (FTIR) technique; quartz was found to be the major mineral (average 59 wt %) with lesser minor amounts of clays. An average grain size of 190μm was obtained from a thin-section image of Tennessee sandstone taken under polarized light.

Mercury injection allowed us to determine the pore-throat size distributions. Figure 21 shows the lab measurements conducted on a core plug. We conclude that the pore-throat size distribution in the network of the connected pores is random because the trend of the capillary pressure with wetting-phase saturation is plateau-like. The trend of the capillary pressure with non-wetting phase saturation (= 1 – wetting-phase saturation) is also plateau-like, but we illustrate the former one as it is more common.

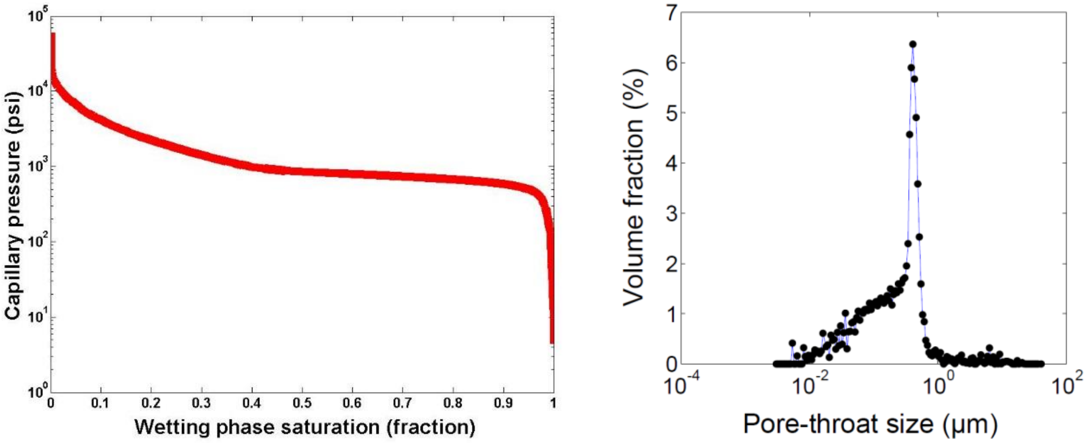

Figure 21 – (a) Capillary pressure measurements of a Tennessee sandstone shows a plateau-like trend, which is consistent with a random pore-throat size distribution in the network of connected pores. (b) Pore-throat size distribution of the sample is determined based on the Young-Laplace relation. (Reproduced from Damani, 2013)

The pore-throat size distribution is determined using the capillary pressure measurements (b). The capillary pressure is increased incrementally, and the injected fluid volume at each increment is measurement. The incremental volume indicates the pore volume associated with a specific pore-throat size, which is determined from the applied capillary pressure. The volume fraction of each pore-throat size is equal to the ratio of the injected mercury volume to the pore volume, and the pore-throat size is a function of the capillary pressure, based on the Young-Laplace relation (eq. 4). The interfacial tension of mercury is 487 x 10^{-3} (N/m), and its contact angle is 140^0.

The network modeling approach is used here to simulate the intact pore space of the Tennessee sandstone. In network modeling, the pore bodies (sites) are interconnected via pore-throats. The flow rate between adjacent sites is determined as follows:

$$q = g_{hydraulic}\Delta \mathrm{p} = \frac{\Pi r^4}{8\mu L}\Delta \mathrm{p} \tag{6}$$

Where q is the flow rate, $g_{hydraulic}$ is the hydraulic conductance of a connecting pore-throat, Δp is the pressure difference between sites, r is the pore-throat radius (Eq. (4)), L is the pore-throat length, and μ is the fluid viscosity.

We created a two-dimensional regular lattice model, with 500 x 1200 throats, to mimic the intact pore space. The spatial distribution of the pore-throat size is randomly distributed in the network model. To determine the permeability, we apply a pressure gradient across the large-scale (network) model and assume that the mass is conserved at each site. The flow rate, which is computed under steady-state conditions, as the entrance of the large-scale model allows us to determine the permeability based on Darcy's law.

The pore-throat length is 190 µm, which makes the network size equal to 95 mm x 228 mm. The thickness of the model is tuned such that its porosity becomes equal to 5.5 %, which is measured in the lab. These parameters lead to a network model, whose volume is equal to 1 cm^3. The permeability of the tuned network model becomes equal to 4 md, which is consistent with the measured permeability. The network model is physically representative of the intact pore space because it can predict the measured permeability when its porosity and the pore-throat size distribution are representative of the formation.

The developed pore model is two-dimensional while the sample is three-dimensional. The model is suitable only because it can capture the petrophysical measurements conducted on core plugs; it has sufficient complexity to mimic the pore-scale processes. Two reasons can be given to justify the difference between the dimensions. First, the network model is simply a tool to account for the effective connectivity of the sites and their interactions. The spatial distribution of the sites can be changed to form a three-dimensional structure. Second, the two-dimensional model may be accurate for a representative slice of the actual pore space. A three-dimensional model can be generated from a representative slice. Thus, it is sufficient to study only the representative slice of the sample, rather than the actual three-dimensional sample.

3.3 Hydraulic fracturing of a Tennessee sandstone block

We cut and polished a cylindrical Tennessee sandstone and stimulated the block-scale sample under triaxial loading conditions. The sample diameter was 4 in, and its length was approximately 5-1/2 in. A hole of ¼ inch in diameter was drilled in the center of the core and extended up to half the sample length. The hole was completed with a ¼ inch OD tube that was cemented (Damani, 2013).

Triaxial stress (vertical stress = 3000 psi, maximum horizontal stress = 2000 psi, minimum horizontal stress = 500 psi) was applied to replicate the in-situ stress conditions. The loading system was designed to allow triaxial loading of the rock sample with simultaneous injection of fracturing fluid and recording of acoustic emissions. The three stresses were applied using confining fluid pressure, hydraulic flat jacks, and an axial piston (Figure 22).

Figure 22 – Hydraulic fracturing lab experimental setup. The figure on the left shows an expanded view of the triaxial loading system with axial loading, confining vessel and flat jacks to apply transverse stress. The figure on the right shows the sample covered with copper jacket mounted on the base plate of the triaxial loading system. (Damani et al., 2012; Damani, 2013).

Oil was then injected into the hole at a rate of 10 cm^3/min. The pressure starts to increase in the hole, and the fluid diffuses into the pore space of the rock. Consequently, localized microcracking is initiated in the rock and with continued oil injection, the microcracks start to coalesce and form a large fracture. The block breaks down at 4336 psi, which was indicated by a sharp fall in the pump pressure.

The AE events can be divided into pre- and post-breakdown events. Pre-breakdown events may be caused by rock failure due to stress induced by wellbore pressurization and the injected fluid diffusing locally into matrix whereas post-breakdown events may be caused by flow through the fracture and failure of asperities along the fracture faces. In our experiment, most events were post-breakdown events (Figure 233).

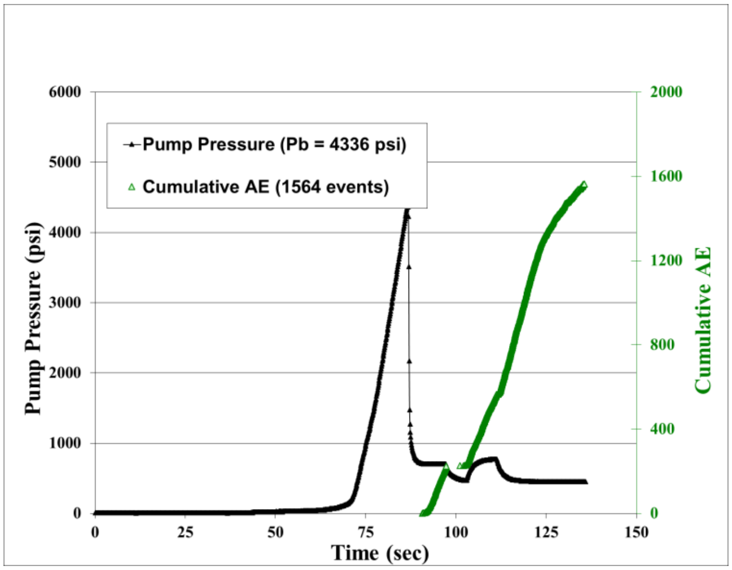

Figure 23 – Pump pressure and cumulative AE events with time (Reproduced from Damani, 2013)

There were 16 piezoelectric sensors mounted on the block, with one on the top, one on the bottom, and the remaining 14 on the cylindrical surface of the sample, distributed uniformly over the azimuth and the height. AE events showed a delayed response, with the first events being captured at the breakdown and after that increasing rapidly. The average error in hypocenter locations for this test was +/-5.34 mm, and the amplitude of the events ranged from 0.1 to 0.9 V. The total number of events was equal to 1564, and the density was higher close to the large fracture (Figure 244). To locate the AE events, the individual arrival times of the compressional waves associated were recorded automatically. The first arrivals were used to determine the event location using a weighted least squares inversion algorithm (Damani, 2013). A frequency of 50 kHz to 1.5 MHz was used to filter the good events; the rest of the events with frequencies outside the range were treated as noise.

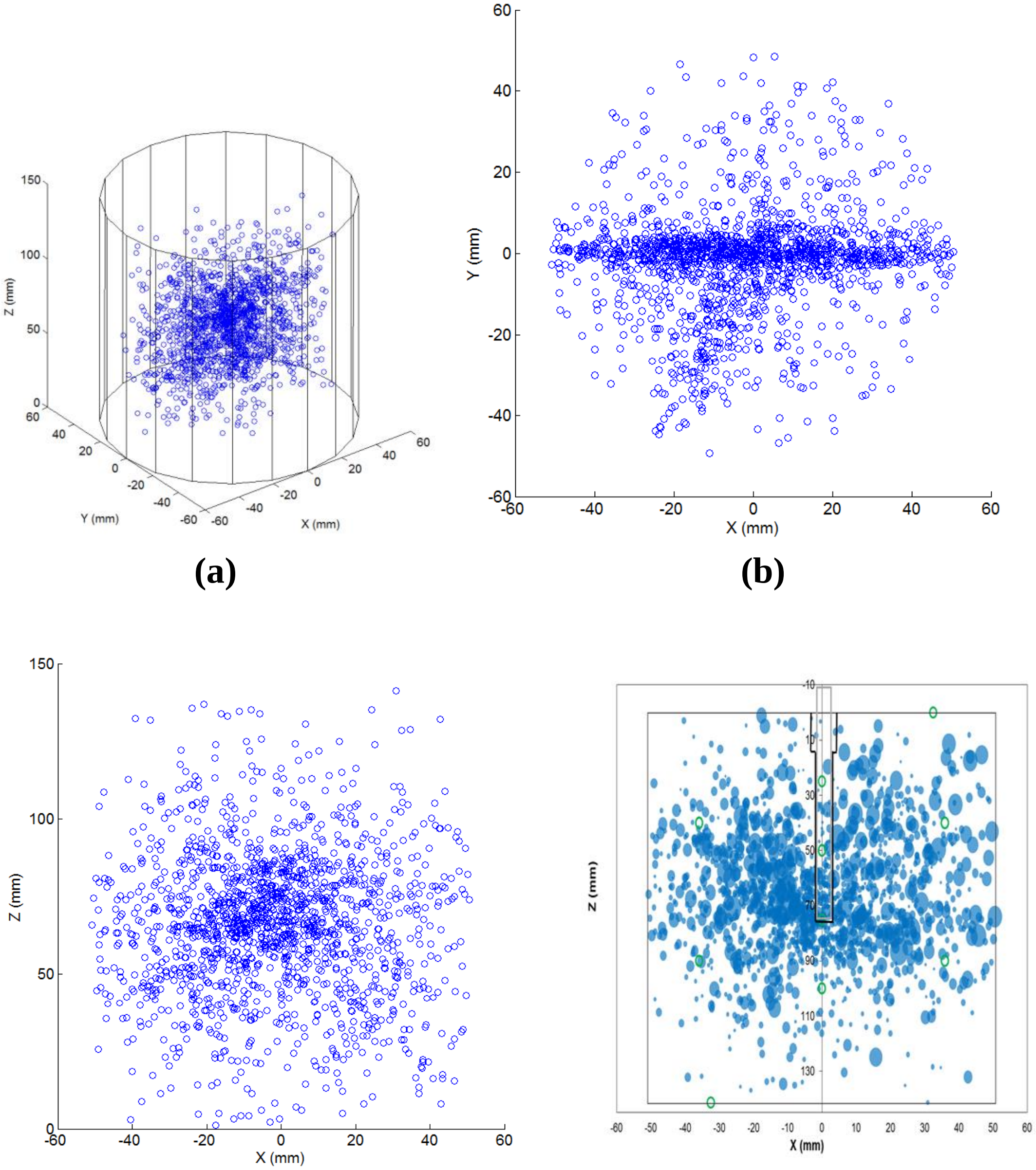

(a)

(b)

(c)

(d)

Figure 24 – Spatial locations of 1564 AE events recorded during hydraulic fracturing of a Tennessee sandstone block in an (a) three-dimensional coordinate system, (b) X-Y plane, and (c) X-Z plane. (d) The size of the blue bubbles corresponds to the amplitude of the AE events. The green circles represent the sensor locations. (Reproduced from Damani, 2013)

3.4 Integrating acoustic emission into percolation theory to predict permeability enhancement

In this chapter, we use the percolation theory to predict the permeability enhancement of the formation at the core scale. It clarifies how the percolation theory can relate AE events to the high-permeability paths created in the formation stimulation.

Percolation takes place when one medium spreads randomly through another (Berkowitz and Ewing, 1998). Examples include the diffusion of a solute through a solvent, disease spreading in a society, and fluid spreading in a porous medium (Broadbent and Hammersley, 1957). Randomness is the key feature of percolation theory and arises due to different mechanisms that are relevant to the penetrating and penetrated media (Sahini and Sahimi, 1994).

Figure 255a shows a network model where the black circles and the dashed lines indicate the absence of the fluid. The red squares and the solid lines indicate the presence of the fluid. The percolation takes place when the fluid forms a connected-through path in the model. The connected-through path is shown in red in Figure 255b.

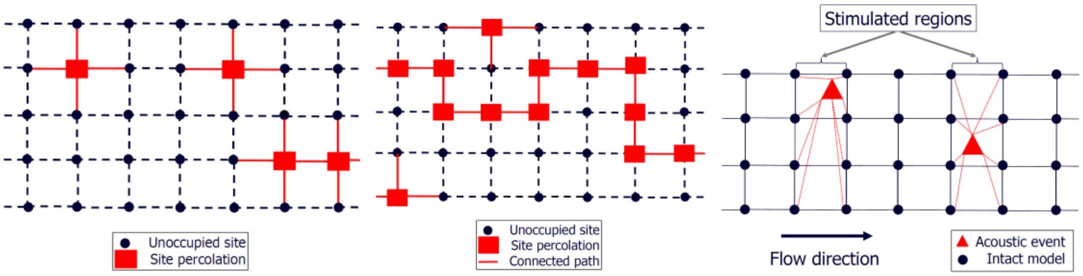

(a) (b) (c)

Figure 25 – (a) Site percolation where the pore body (site) is filled randomly by the fluid. The black color corresponds to the absence of the fluid. (b) Shows a condition where percolation takes place, and there is a connected-through path from the left to the right of the model. (c) A conceptual model for pore-scale modeling of an AE event. The AE events are assumed to be indicators of micro-fractures that interact with the adjacent pore bodies of the intact pore space.

The number of the sites occupied by the fluid relative to the total number of sites is equal to the probability (*p*), which is equal to unity when the fluid fills all the sites and to zero when there is no fluid in the model. The probability of the model is equal to the percolation threshold when percolation takes place (Dean and Bird, 1967). The number of the occupied sites exceeds a certain number when the probability becomes equal to percolation threshold. Figure 255b shows a network model where the fluid occupies different sites randomly, and the percolated path is shown in red in Figure 255b where the fluid forms a path from the left to the right of the model.

We use a physically representative pore model to implement the effects of the microfractures on the transport properties. The pore space is treated as a network of pore bodies (sites) that interact with each other through pore-throats (Figure 255c). Each event in the representative volume is indicative of a large pore body, shown as a red triangle in Figure 255c. The larger pore body, whose volume is equal to the void space that resides in the microfracture, is connected to adjacent pores via pore-throats, shown with dashed red lines. The transport properties of the pore-throats connected to the large pore are dependent on the characteristic size of the microfracture.

The large pore body is distributed randomly as a site, which classifies the problem as a site percolation. Percolation theory predicts large-scale behavior by accounting for randomly interconnecting small-scale phenomena. We assume that the small-scale fractures form a connected-through path when the number of AE events per unit volume exceeds a certain value, which is relevant to the percolation threshold.

The large pores (red triangles in Figure 255c) are connected to all the pores of the intact pore space (black circles in Figure 255c) in the stimulated region. Figure 255 is a conceptual illustration, and the permeability calculation based on the proposed method is discussed subsequently (Eq. (7)). The volume fraction of the stimulated regions depends on the number of AE events per unit volume of the representative volume that corresponds to the percolation threshold. For instance, Figure 255c shows a condition where the number of AE events per unit volume of the representative volume is equal to 2, and the large pores form a connected-through path when this ratio becomes equal to 6.

The total volume of the physically representative model is divided into the number of events recorded per unit volume for the fractured plug. The volume fraction of the stimulated region for partially fractured samples is equal to the ratio of its number of events per unit volume to the number of events per unit volume for the fractured plug.

Chapter 4: Predicting permeability enhancement based on percolation theory

We consider a one-dimensional flow where the stimulated and intact regions act in series, which allows us to determine the core-plug permeability as follows:

$$K_{eff} = \frac{N}{\frac{n}{K_f} + \frac{N-n}{K_m}} \tag{7}$$

Where K_{eff} is the effective permeability of a partially fractured plug, K_m is the matrix permeability of an intact sample, K_f is the permeability of a fully fractured plug, N is the total volume of the model, and n is the stimulated region volume.

The physically representative model is used here to predict the permeability enhancement at the core scale. The number of AE events per unit volume (#Events/volume) is determined for a core plug that has a large fracture, which can be observed with the naked eye. This ratio corresponds to the percolation ratio when the fracture forms a connected-through path. The permeability measurements of other core plugs, extracted from the stimulated block, provide independent evidence to test the model.

We extracted five core plugs from the stimulated Tennessee sandstone block for petrophysical characterization (Figure 266). One plug was extracted right on top of the large fracture (Left wing in Figure 266a), whereas the other four plugs were extracted from either side of the large fracture (Right Wing in Figure 266a). Figure 266c shows a scanning electron microscope (SEM) image of the formation where there is a connected-through fracture in the sample, which is created during hydraulic fracturing of the block. The high-resolution image shows the fracture with no confinement. The high-resolution suggests that the aperture size of the connected fracture could be on the order of 1-10 µm.

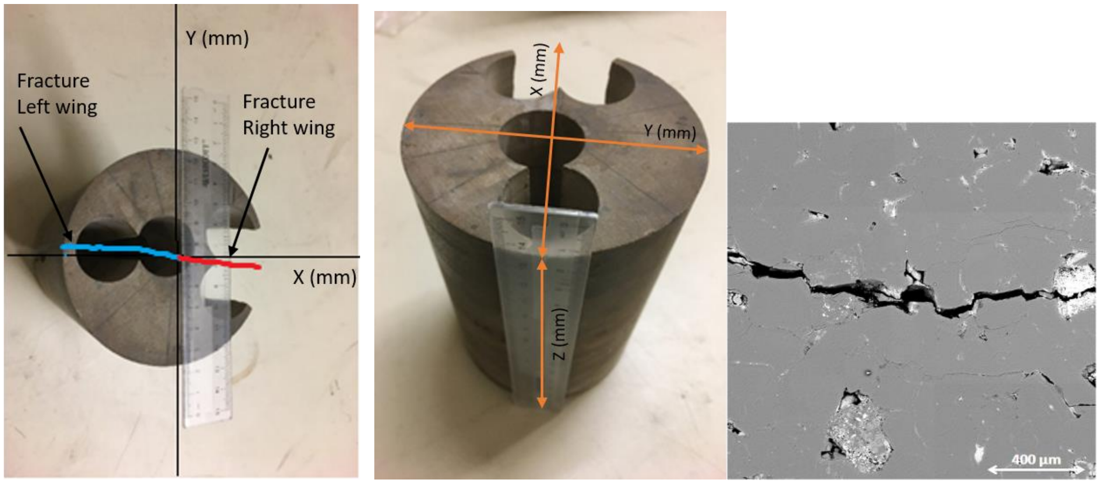

(a) (b) (c)

Figure 26 – (a-b) Block-scale sample of a hydraulically fractured Tennessee sandstone, where the holes show the locations of the extracted core plug for permeability measurements. The fracture left, and right wings are shown by blue, red lines, respectively. (c) Scanning electron microscope (SEM) image of the fractured core plugs that shows a connected-through fracture in the sample. (Reproduced from Damani, 2013)

Table 1 lists the spatial locations of the core plugs for the coordinate system shown in Figure 266, their bulk volume, and the number of AE events. The core plug with the connected-through fracture is referred to as the Fractured plug in Table 1 and has the largest #Events/volume and highest permeability; the other plugs are named Plugs 1-4 in Table 1.

Table 1 – Spatial location, number of AE events, and the block volume of the core plug extracted from the stimulated Tennessee sandstone block shown in Figure 266.

Plug	X(mm)	Y(mm)	Z(mm) Top	Z(mm) Bottom	Bulk volume (cm^3)	AE/volume (cm^{-3})
Plug 1	30	12.5	0	31	15.21	0.13
Plug 2	30	12.5	31	58	15.21	0.79
Plug 3	30	-12.5	0	31	13.25	0.45
Plug 4	30	-12.5	31	58	13.25	1.58
Fractured plug	-32	0	39	78	19.27	6.95

Table 2 – Plug length, diameter, and permeability at 300 psi effective stress

Plug	Length (mm)	Diameter (mm)	Permeability (md)
Plug 1	31	25.4	0.008
Plug 2	27	25.4	0.007
Plug 3	31	25.4	0.007
Plug 4	27	25.4	0.007
Fractured plug	39	25.4	8.097

We measured the permeability of each core plug listed as a function of effective stress (Table 2). The confining stress was changed where the pore pressure was 200 psi. The pore pressure was fixed using the AP-608^{TM} permeameter, and the effective stress was calculated as follows:

$$Effective\ stress = Confining\ stress - Pore\ pressure \tag{8}$$

The lab measurements are normalized with respect to the measured value for each sample when the effective stress is equal to 300 psi (Figure 277). The results are normalized with respect to the confined conditions because they are more representative of in-situ conditions. The rate of the permeability decrease with the effective stress is relatively similar for different samples, especially at low effective stress. The similarity suggests that the permeability decline is controlled by the change in the effective aperture size of the fractures. The similarity could also be a result of homogeneous material distribution. The decrease rate of the fractured plug deviates from the other plugs as the effective stress increases, which could be due to the plastic deformation. The lab measurements revelated that the plug permeability did not recover fully to the original value because of the plastic deformation after the test when the confining stress was removed.

The fractured plug permeability was also measured as a function of the confining stress. The fractured plug permeability was 5.342 md when the confining stress was equal to 1000 psi. The measured permeability is used as an estimate of the permeability of the stimulated region (Figure 255c). The measured permeability is also used to normalize the results, denoted by $k_{\text{fractured plug}}$ in Figure 288.

The spatial locations of the recorded events and the bulk volume of each core plug determine the number of AE events per unit volume (#Events/volume). This ratio is equal to 6.95 cm^{-3} for the fractured plug, which corresponds to the percolation threshold. We predicted the permeability of the core plug when this ratio is smaller than the percolation threshold based on percolation theory, using the physically representative pore model. Figure 288 reveals the core-scale measurements corroborate the predicted results. The permeability of the formation remains close to the intact value at the core scale when the #Events/volume is smaller than the threshold value. Our model also suggests that the stimulated permeability increases by a factor of 2 relative to the intact permeability (=4md). Thus, the intact permeability remains close to the matrix permeability, as opposed to the fractured plug permeability.

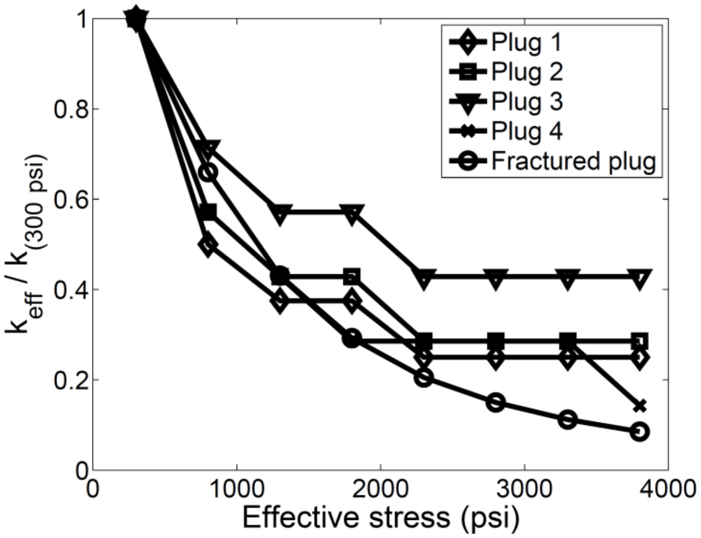

Figure 27 – The permeability decreases as the effective stress increases for different plugs.

We used all the data available from the core plugs recovered from the block sample to test our model. Most AE events occur on the fracture, which is the reason for the absence of lab measurements with #Event/volume between 3 and 6. The core plugs with small #Events/volume were taken as close as possible to the main fracture. Nonetheless, the stimulation results and lab measurements indicate that the permeability close to the main fracture remains close to the intact permeability and the enhanced permeability does not increase linearly with #Events/volume.

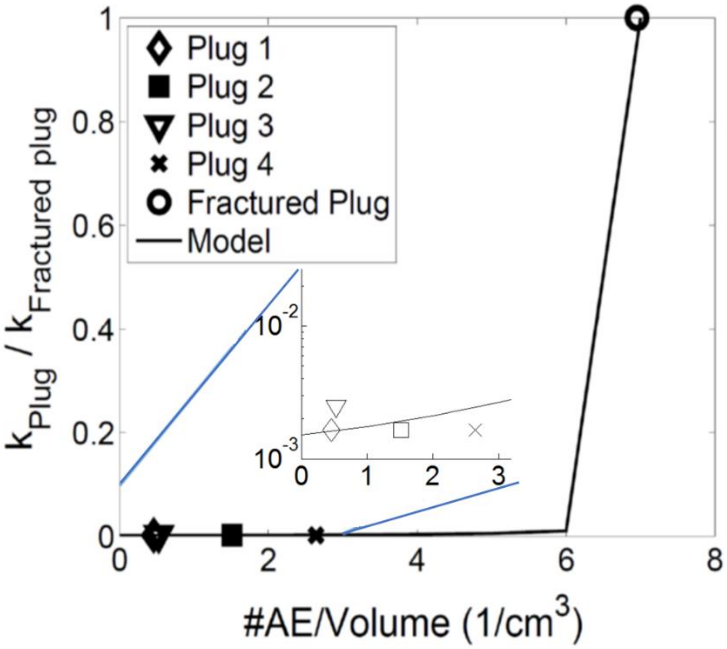

Figure 28 – Core-scale measurements corroborate the physically representative pore model, which predicts the permeability enhancement based on percolation theory. The stimulated permeability remains very close to that of the matrix, as opposed to that of the fractured plug, when the number of AE events per unit volume (#AE/volume) is smaller than the percolation threshold.

Now, we turn to the sensitivity of the results to the amplitude cutoff (%) (Figure 299). The amplitude cutoff (%) is defined as removing events that have amplitude value in the bottom x% of the total events. The number of events per unit volume

(#Events/volume) decreases the most for the fractured plug. The significant decrease for the fractured plug indicates that there is a wide amplitude range. Nevertheless, it is apparent that the cutoff value does not change the trend of results because it only shifts them monotonically.

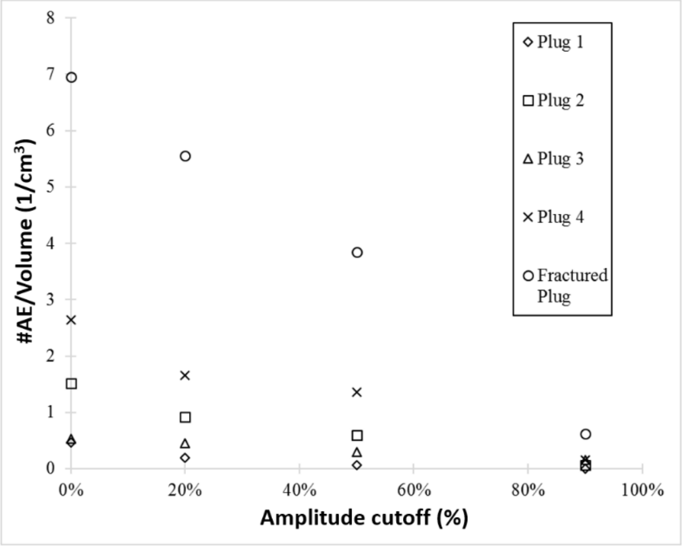

Figure 29 – #Events/volume decreases monotonically with increasing amplitude cutoff (Reproduced from Damani, 2013)

Dahi Taleghani and Lorezo (2011) indicated that low-frequency events are the tensile events causing Mode I failure. Low-frequency events are beyond the scope of the present work because our device does not record events below 50 kHz. We considered four kinds of failure mechanisms: shear, tensile, compressive, and complex.

Chapter 5: Workflow for predicting breakdown pressure and breakdown cycle in cycling fracturing

5.1 Cyclic fracturing of the Tennessee sandstone sample

Our objective in this part of study is to predict the reduction in the breakdown pressure in cyclic fracturing in the context of petroleum engineering. Our objective is not to prove the existence of this phenomenon, which has been tested in other engineering fields for half a century (Paris et al. 1961). The existence of this phenomenon has also been confirmed recently at the lab scale, but its design and prediction have remained limited to trial and error (Patel 2017). Providing a predictive model for this phenomenon will facilitate further discussion about improving the conventional method, which could have major implications for improving hydrocarbon recovery. To reach our objective, we use all the data available in the literature for low-cycle fracturing. The existing lab measurements are limited simply because this is a new concept in petroleum engineering. Conducting further measurements is beyond the scope of the present study.

The lab measurements (Patel et al., 2017) are discussed for completeness. The Tennessee sandstone samples were first cut cylindrically and polished. Table 3 lists the petrophysical properties of each sample. The sample diameter and length were 4 in and 5.5 in, respectively. A hole of ¼ inch in diameter was drilled in the center of the core and extended up to half the sample's length. The hole was completed with a ¼-inch diameter tube that was cemented. To replicate the subsurface conditions, triaxial stress was applied (vertical stress = 3000 psi, maximum horizontal stress = 2000 psi, minimum horizontal stress = 500 psi). Figure 22 shows the experimental setup.

Table 3 – Porosity and permeability of the Tennessee sandstone samples analyzed here. Lab measurements are based on the data available in the literature (Patel et al. 2017).

Sample	Porosity (%) (500 – 4000 psi)	Permeability (μd) (500 – 4000 psi)
1	4.7 – 4.3	27 – 7
2	5.1 – 4.4	32 – 9
3	4.4 – 3.6	37 – 10
4	5.9 – 6.1	22 – 11

The lab measurements include four dry samples. The first two were stimulated using the conventional method by increasing the pump pressure monotonically. The other two were fractured via cyclic loading. Table 4 lists the breakdown pressures for the samples that were stimulated with an oil injection rate of 10 cm^3/min.

Table 4 – Breakdown pressures and number cycles of four Tennessee sandstone samples under triaxial loading conditions (vertical stress = 3000 psi, maximum horizontal stress = 2000 psi, minimum horizontal stress = 500 psi)

Sample	Fracturing method	Breakdown pressure (psi)	Number of cycles
1	Conventional	2947	1
2	Conventional	3067	1
3	Cyclic	2519	7
4	Cyclic	2900	5

We define the reference breakdown pressure (= 3007 psi) for the conventional method as the average breakdown pressures (Samples 1 and 2 in Table 3). The maximum first injection pressures are equal to 322 psi for Sample 3 and 1621 psi for Sample 4 (Figure 3030). Subsequently, the maximum injection pressure of each cycle was increased by 10% of the reference breakdown. The minimum pump pressure in each cycle for both samples was 15 psi. The breakdown pressure is smaller in the cyclic method than in the conventional method.

The reduction in the breakdown pressure depends on the loading path, which includes the number of cycles and the effective pressure. Sample 4 fails after fewer cycles than does Sample 3. The reduction in the breakdown pressure of Sample 3 (16%) is more significant than that of Sample 4 (3%). This could be due to the significant increase in the pump pressure in the first cycle for Sample 3. We will propose a workflow to predict the breakdown pressure (Methodology), which can be used for both samples. We will also present different scenarios which could be used to lower the breakdown pressure more significantly. The workflow allows us to predict the breakdown pressure for both samples (3 or 4) when one of them is used to tune the model. The discussed experiments require block-scale (bench-scale) samples whose size is close to 4 in. It is not possible to conduct those tests on shale samples because they disintegrate before the tests' completion.

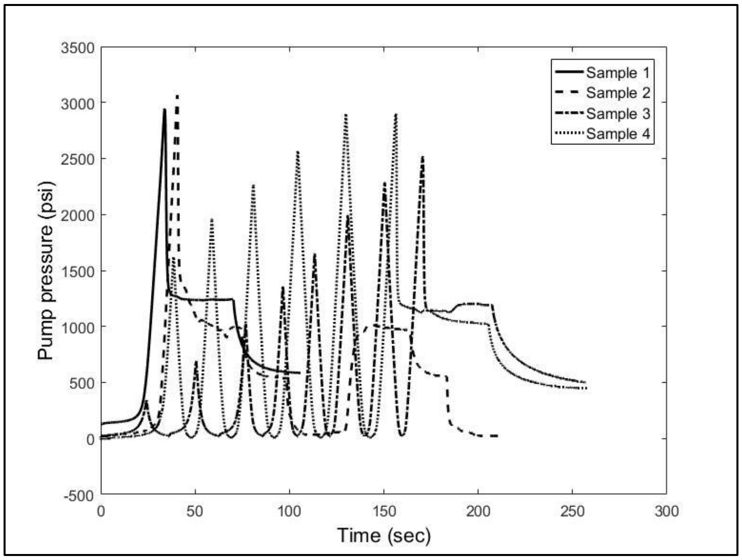

Figure 30 – Pump pressure data show that Samples 1 and 2, which were conventionally fractured, have higher breakdown pressures than do the cyclically fractured samples (3 and 4). The breakdown pressure of Sample 4 is higher than that of Sample 3 but requires fewer cycles to fail. (Reproduced from Patel et al., 2017)

The rock sample breaks down at a lower pressure in cyclic fracturing than in the conventional method because of the local damage (crack growth) in each cycle. Figure 31 shows that there are more acoustic emission (AE) events in cyclic fracturing. The increase in the number of events provides independent evidence for the creation (or growth) of small-scale cracks.

The higher number of AE events in cyclic fracturing corresponds to a larger stimulated reservoir volume. This is an important advantage of cyclic fracturing compared to the conventional method—each event may be correlated with a small fracture, which leads to a larger permeability for the stimulated region. The formation permeability at the core scale was not measured at different locations for the analyzed tests. Thus, the stimulated volume is larger in cyclic fracturing, although it is not currently possible to evaluate the corresponding permeability.

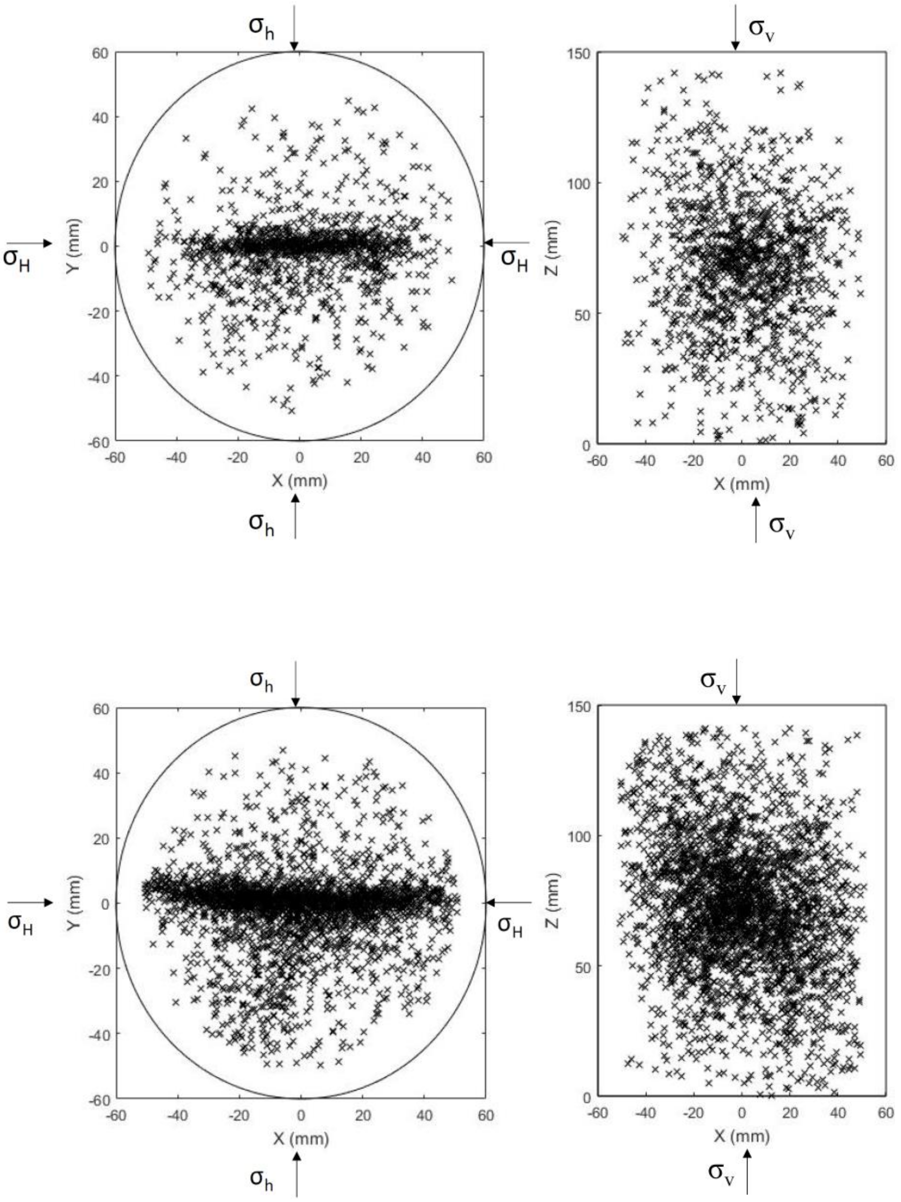

Figure 31 – The number of acoustic emission (AE) events is higher in cyclic fracturing (bottom) than in conventional fracturing (top), which suggests that the stimulated reservoir volume is larger in cyclic fracturing. The triaxial stresses were σ_v (vertical stress) = 3000 psi, σ_H (maximum horizontal stress) = 2000 psi, and σ_h (minimum horizontal stress) = 500 psi. (Reproduced from Patel et al., 2017)

5.2 Methodology

We use a modified Paris' law that accounts for the fracture closure (Elber 1971) to determine the crack growth in cyclic fracturing. Paris' law is often used for high-cycle failure (HCF), but we apply it to a low-cycle regime because there is no other model for this range, to the best of our knowledge. The modified Paris' law can be expressed as follows:

$$\frac{da}{dN} = C(U\Delta K)^m \qquad U = 0.5 + 0.4R \qquad R = \frac{K_{min}}{K_{\mathrm{m}}} \tag{9}$$

Where a is the crack length, N is the number of cycles, ΔK is the change in the stress intensity factor, C and m are constants, U is the Elber constant, and R is the loading ratio. The change in the stress intensity factor (ΔK) is equal to the difference between the minimum stress intensity factor (K_{min}) and the maximum value (K_{max}).

We propose a workflow (Figure 3232) to tune the modified Paris' law. The modified Paris' law has three unknowns (m, C, and initial crack length a_i). The typical range of m is from 0.01 to 30, that of C is from (10^{-1} to 10^{-25}) $\frac{m}{[m\sqrt{Mpa}]^m}$, and the initial crack length is from 0.01 mm to 0.2 mm. The unknown parameters are determined as follows:

1. The fracture toughness (K_{IC}) of a sample is assigned using the data available in the literature. Our study is based on Tennessee sandstone whose fracture toughness was reported by Atkinson (1979).

2. The acceptable range of each unknown parameter in the modified Paris' law is determined (C, m, and a_i) based on the data available in the literature. A combination of (C,m, ai) are picked from this range to begin.
3. The highest effective stress in each cycle is used to determine the crack growth in each cycle using the Paris' law (Eq. 9). We determine the crack growth for Sample 3 in our study until breakdown cycle. (Table 4)
4. The stress intensity factor at the breakdown cycle and the maximum breakdown pressure are used to determine the effective breakdown stress intensity (K_b). The effective breakdown stress intensity factor in our study is set equal to the first mode intensity factor (K_I).
5. K_b is compared to K_{IC}. If they are not equal, then the unknown parameters (C, m, and a_i) are changed, and steps 3,4 are repeated until K_b becomes equal to K_{IC} at the breakdown pressure and breakdown cycle. The combination of the unknown parameters whose corresponding K_b is equal to K_{IC} defines a tuned Paris' law.

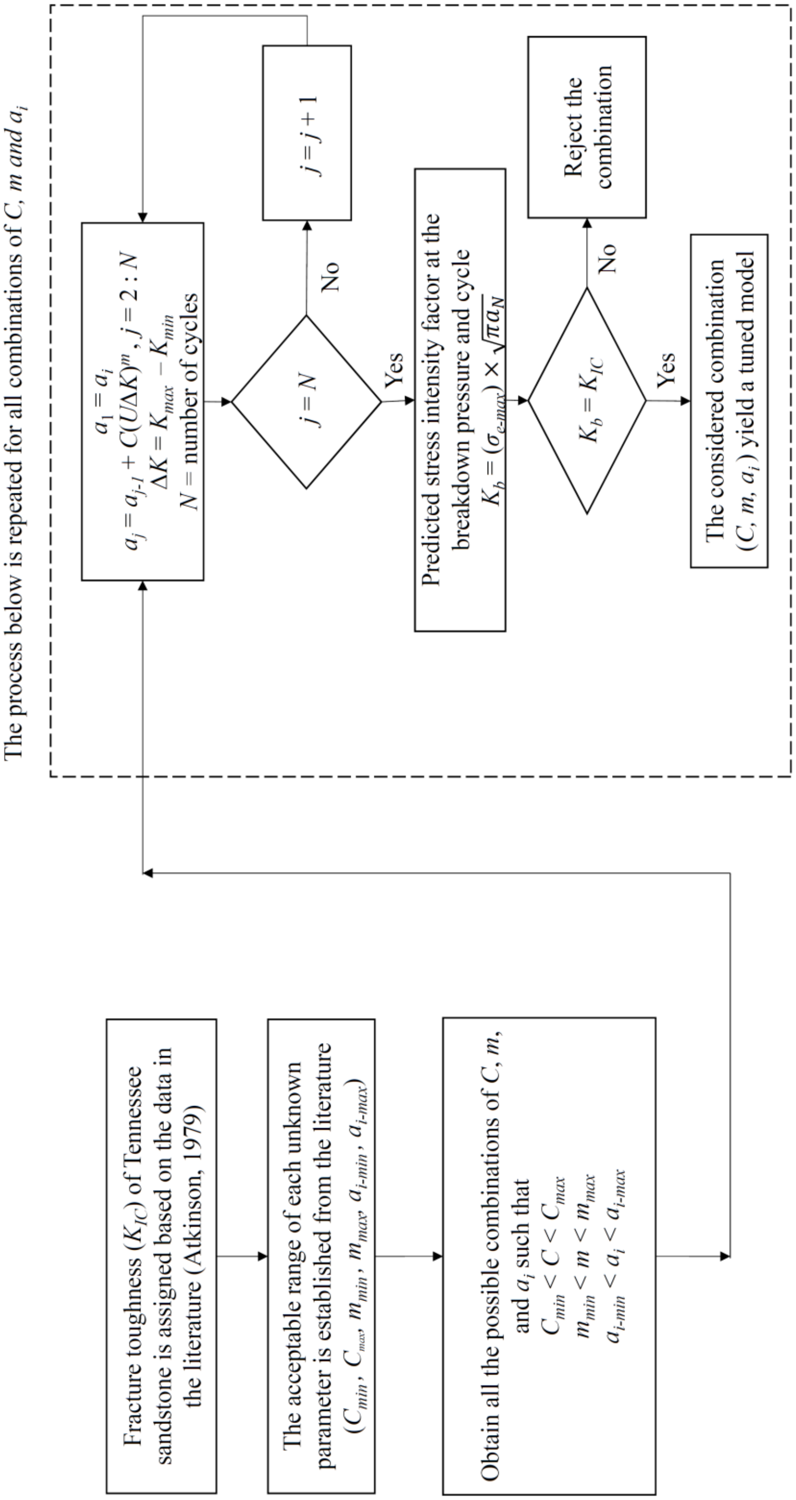

Figure 32 – Flowchart to determine the unknown parameters (*C*, *m*, and a_i) in the modified Paris' law (Eq. 9). The tuned model, whose accuracy is tested for Sample 4, helps us to predict the breakdown pressure and cycle.

Chapter 6: Predicting breakdown pressure and breakdown cycle in cycling fracturing

We use the modified Paris' law to predict the breakdown pressure and the cycle for Tennessee sandstone samples. The unknown parameters (*C*, *m*, and a_i) are determined based on the proposed workflow (Figure 32) using the cyclic fracturing data of Sample 3. Subsequently, we use the tuned model to predict the breakdown pressure for Sample 4. The fluid pressure at each cycle and the number of cycles for Sample 4 are different from those of Sample 3. The error associated with using the tuned model is determined as follows:

$$\text{Error (\%)} = \left|\frac{K_b - K_{IC}}{K_{IC}}\right| \times 100 \tag{10}$$

Where K_b is the effective breakdown stress intensity factor that is predicted using the tuned model and K_{IC} is the fracture toughness. The predicted stress intensity factor is representative of the maximum pressure for a cycle in which the sample fails.

Now, we turn to the error associated with using the tuned model to predict the breakdown pressure only for Sample 4. Figure 333 shows that the error remains smaller than or equal to 15% with different combinations of parameters. There is no unique solution based on the proposed workflow for the observed (good) accuracy. Figure 333 allows us to test the second hypothesis. It shows that the modified Paris law can predict the breakdown pressure and breakdown cycle in low-cycle fracturing.

The workflow allows us to predict the breakdown pressures of both samples (3 or 4), with the same level of accuracy, when one of them is used to tune the model. The good accuracy of the results, when compared with the data available in the literature, corroborates the proposed workflow.

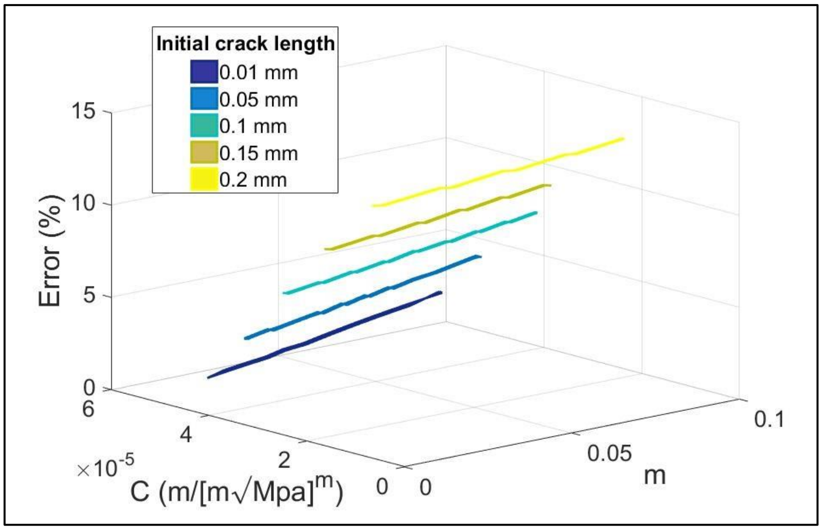

Figure 33 – Error (Eq. 10) in predicting the breakdown pressure for cyclic fracturing for Sample 4. The unknown parameters in the modified Paris' law are determined based on the workflow provided in the Methodology for Sample 3.

The tuned model helps us to predict the breakdown pressure and cycle for different scenarios. Both are unknown a priori. The fluid pressure in each cycle can also change independently. The failure takes place when the difference between the predicted effective stress intensity factor and the fracture toughness becomes negligible. Two scenarios are considered where the fluid pressure is changed cyclically. In the first scenario, the fluid pressure is increased at 400-psi increments, and in the second, the fluid pressure increment is equal to 200-psi. Figure 344 shows the predicted results, where the sample with smaller pressure increments fails at a lower pressure but a larger number of cycles.

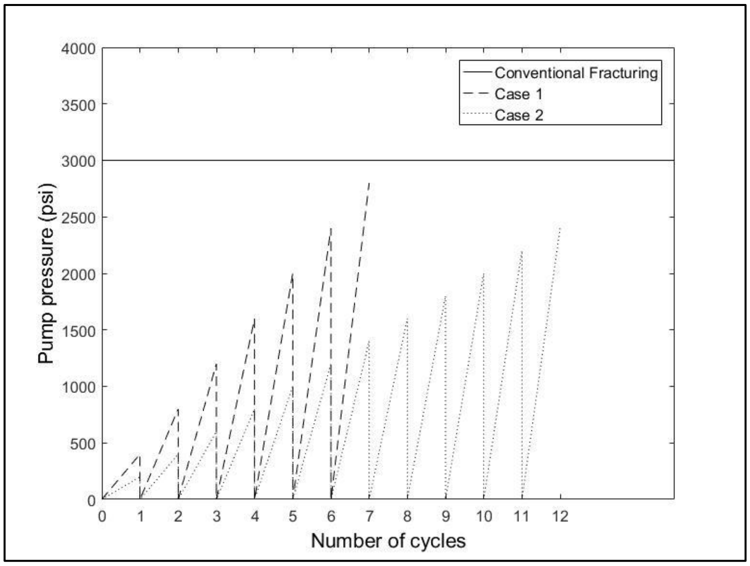

Figure 34 – Predicted failure for two scenarios based on the tuned model: Case 1 shows a higher breakdown pressure at a lower number of cycles than does Case 2.

Chapter 7: Discussion and future works

7.1 Pore-scale modeling of acoustic emission (AE) events

In petroleum engineering, the goal of most research including the present study is to be applied in the field. The presented model and lab measurements predict the permeability enhancement of a stimulated region, without a connected-through fracture, based on its acoustic emission. The stimulated region is also referred to as the process zone (Zang et al., 2000). Our study suggests that the enhanced permeability remains close to the intact permeability and that it is unrealistic to use a linear approximation for the stimulated region permeability. Knowing that, in the absence of a connected-through fracture, the permeability increase is not very significant is crucial for building a realistic reservoir model.

Another issue is the size of the stimulated region. The size of the stimulated region, whose permeability is close to the intact permeability, relative to the overall domain is equal to the size of the core plug to the block. We can predict the stimulated region size if the results can be scaled to the field conditions. The stimulated region size close to each fracture can be predicted by accounting for the fracture length.

The presented results are relevant to fluid injection into a dry sample. The size of the stimulated region and the spatial distribution of the events may change if the sample is initially saturated and when conducted for a different formation. Our model assumes that the spatial distribution of the pore-throat size is random, which is realistic for Tennessee sandstone. The developed model needs modifications when this assumption is not realistic.

7.2 Cyclic fracturing

The cyclic fracturing has positive and negative effects. The number of acoustic emission (AE) events increases in cyclic fracturing (Figure 31Figure 31), which corresponds to a larger stimulated volume (positive). The cyclic fracturing requires more fluid volume and energy than does conventional fracturing (negative). The existence of opposite effects implies that there may be an optimum scenario where achieving the enhanced properties of the stimulated volume through cyclic fracturing is better than through re-fracturing. Designing the optimum scenario requires analyzing both effects. The required lab measurements for the quantitative assessment of the positive effect are not available, and thus we analyze the negative effect.

In cyclic fracturing, the fluid pressure is increased and decreased cyclically until breakdown takes place. This is carried out by injecting fluid into the sample and monitoring pump pressure; thus, more fluid is injected in cyclic fracturing. Table 5 lists the required fluid volume for each test.

Table 5 – Fluid volume, breakdown pressure, and energy of different hydraulic fracturing methods.

Sample	Number of cycles	Injected fluid volume, ml	Breakdown pressure, psi	Energy, kJ
1	1	5.6	2947	145
2	1	6.7	3067	115
3	7	28.4	2519	502
4	5	26	2900	728

The injected volume, which corresponds to before the breakdown period, is approximately 340% higher in cyclic fracturing than in the conventional method for the Tennessee sandstone samples. The fluid leak-off decreases when the permeability is smaller for a given period. Thus, the difference between the injected volumes of the cyclic and the conventional methods is expected to be smaller in tight formations than the results listed in Table 5.

We also compare the required energy for both methods (cyclic and conventional). The energy calculation is based on the pump pressure, the injected fluid volume at a given pressure, and the time interval. It is apparent that the cyclic fracturing requires more energy for the formation stimulation (Table 5). This is a disadvantage of the cyclic fracturing method, compared to the conventional approach. The difference between the required energy is expected to be less significant for tight formations, as the difference between the injected volumes is smaller.

The cyclic fracturing method has the potential to become a new stimulation method after its advantages and disadvantages are quantitatively accounted for, especially when the optimum scenario is designed. The proposed workflow (Figure 32) facilitates further discussion to determine its feasibility by predicting the breakdown pressure and cycle. The breakdown pressure in the field, which is not necessarily equal to the measured value in the lab, needs to be determined for such applications. In the field, the breakdown pressure may exhibit a large variation. The diagnostic fracture injection test (DFIT) can provide an estimate of the breakdown pressure in the field (Barree et al. 2015).

Chapter 8: Conclusions

Hydraulic fracturing is one of the most important inventions in the petroleum industry because it has made hydrocarbon production from tight formations possible. It has launched a new era with major consequences, some of which may become clear in years or decades to come. This implies that a slight improvement in hydraulic fracturing can have a major impact.

8.1 Pore-scale modeling of AE events

We developed a physically representative pore model of an intact Tennessee sandstone at the core scale by analyzing its permeability, porosity and capillary pressure measurements. Our main objective was to predict the permeability enhancement by accounting for acoustic emission (AE) events. We assumed that each event is representative of a microcrack or is indicative of an asperity which compressed during fracture closure. This assumption implies that a connected-through fracture is formed when the number of AE events per unit volume becomes larger than the threshold value.

We predicted the permeability enhancement of a formation based on percolation theory. Our study shows that the stimulated permeability of a formation at the core scale is much smaller than the fractured plug permeability if the number of events per volume is smaller than the threshold value. The permeability enhancement of the core plug, relative to intact conditions, is close to 2 when the fracture does not form a connected-through path. The proposed model, which relates the number of acoustic emission events to the enhanced permeability based on percolation theory, has major applications in determining the transport properties of the stimulated reservoir volume.

8.2 Cyclic fracturing

In the present study, we proposed a new method for predicting the breakdown pressure and the number of cycles to breakdown in cyclic fracturing. Cyclic fracturing is a new concept in petroleum engineering where the fluid pressure is increased and decreased cyclically to stimulate the formation. This is fundamentally different from the conventional method, where a fracture at each stage is created by a monotonic increase in the fluid pressure (one cycle). The predictive model is based on a modified Paris' law, which uses linear elastic fracture mechanics (LEFM). We determined the unknown parameters of the Paris' law, which was applied for the first time in the context of petroleum engineering. The predictive model, incorporated in a flowchart, allows us to determine the breakdown pressure and cycle. Independent lab measurements show that the proposed model can predict the breakdown pressure to within less than a 15% error, which is promising.

Comparing the breakdown pressures of Sample 3 (7 cycles, P_b = 2519 psia) and Sample 4 (5 cycles, P_b = 2900 psia), the more number of pressure cycles before breakdown, the lower is the breakdown pressure for Tennessee sandstone. Using the tuned Paris law in a predictive mode for the two hypothetical cases, we observe that case 2 (200 psi pressure increments per cycle) has a higher number of cycles and lower breakdown pressure than case 1 (400 psi pressure increments per cycle). Hence, this experimental observation of sample 3,4 is corroborated with the modeling results from the tuned Paris law that there is a higher reduction in breakdown pressure if more pressure cycles are required to reach the breakdown given all other experimental conditions remains the same.

The cyclic fracturing has an advantage and a disadvantage. It leads to a larger stimulated reservoir volume (positive), while it also requires more fluid volume and energy (negative). We interpreted the larger stimulated volume by accounting for the number of acoustic emission (AE) events in cyclic fracturing. We also analyzed the fluid volume and energy required for cyclic fracturing and compared them with those of the conventional method. The injected volume in the cyclic fracturing is 340% higher, and the energy 370% is higher than in the conventional method. The difference is expected to be smaller in tight formations where a smaller fluid volume leaks off for a given time.

The existence of opposite effects of cyclic fracturing implies that there may be an optimum scenario where achieving the enhanced properties of the stimulated volume through cyclic fracturing is superior to the conventional method. The predictive model can help us design different scenarios relevant to different cyclic pressures, which will lead to different breakdown pressures and number of cycles. The predictive model facilitates further discussion in this field, which can lead to an improved stimulation technique, with major applications in the petroleum industry.

References

Adams, N. J., Mitchell, R. F., Eustes, A. W., Sampaio, J. H., & Antonio, A. O. (2017, January). A Causation Investigation for Observed Casing Failures Occurring During Fracturing Operations. In *SPE Hydraulic Fracturing Technology Conference and Exhibition*. Society of Petroleum Engineers.

Al-dhahli, A., Geiger, S., & van Dijke, M. I. (2011, January). Three-phase pore-network modelling for mixed-wet carbonate reservoirs. In *SPE Reservoir Characterisation and Simulation Conference and Exhibition*. Society of Petroleum Engineers.

Atkinson, B. K. 1979, February. Fracture toughness of Tennessee sandstone and Carrara marble using the double torsion testing method. In International Journal of Rock Mechanics and Mining Sciences & Geomechanics Abstracts, 16(1), 49−53. https://doi.org/10.1016/0148-9062(79)90774-5

Balhoff, M. T., & Thompson, K. E. (2004). Modeling the steady flow of yield-stress fluids in packed beds. *AIChE Journal*, *50*(12), 3034-3048.

Balhoff, M. T., & Thompson, K. E. (2006). A macroscopic model for shear-thinning flow in packed beds based on network modeling. *Chemical Engineering Science*, *61*(2), 698-719.

Barree, R. D., Miskimins, J., and Gilbert, J. 2015. Diagnostic fracture injection tests: common mistakes, misfires, and misdiagnoses. SPE Production & Operations, 30(02), 84−98.

Barrufet, M. A., & White Jr, R. J. (1994, January). A waterflood model based upon percolation theory concepts. In *SPE Latin America/Caribbean Petroleum Engineering Conference*. Society of Petroleum Engineers.

Basu, S., Ali, M. Y., Farid, A., Berteussen, K. A., & Mercado, G. (2014). A microseismic experiment in Abu Dhabi, United Arab Emirates: implications for carbonate reservoir monitoring. *Arabian Journal of Geosciences*, *7*(9), 3815-3827.

Behseresht, J. 2008. *Infinite-Acting Physically Representative Networks for Capillarity-Controlled Displacements*. MS Thesis, The University of Texas at Austin, Austin, Texas.

Berkowitz, B., Ewing, R.P., 1998. Percolation theory and network modeling applications in soil physics. Surv. Geophys. 19 (1), 23–72.

Bethe, H.A. (1935). Statistical theory of superlattices. Proceedings of the Royal Society of London. Series A, mathematical and Physical Sciences, 150(871), 552-575

Bohloli, B., & De Pater, C. J. (2006). Experimental study on hydraulic fracturing of soft rocks: Influence of fluid rheology and confining stress. *Journal of Petroleum Science and Engineering*, *53*(1-2), 1-12.

Broadbent, S.R., Hammersley, J.M., 1957. Percolation processes. Math. Proc. Camb. Philosophical Soc. 53, 629–641.

Bryant, S. L., King, P. R., & Mellor, D. W. (1993). Network model evaluation of permeability and spatial correlation in a real random sphere packing. Transport in Porous Media, 11(1), 53–70. http://doi.org/10.1007/BF00614635

Bryant, S. L., Mellor, D. W., & Cade, C. a. (1993). Physically representative network models of transport in porous media. AIChE Journal, 39(3), 387–396. http://doi.org/10.1002/aic.690390303

Chelidze, T. L. (1982). Percolation and fracture. *Physics of the Earth and Planetary Interiors*, *28*(2), 93-101.

Chong, K.P., Carino, N.J., Washer, G., 2003. Health monitoring of civil infrastructures. Smart Mater. Struct. 12 (3), 483.

Dahi Taleghani, A., Lorenzo, J.M., 2011, January 1. An Alternative Interpretation of Microseismic Events during Hydraulic Fracturing. Society of Petroleum Engineers. https://doi.org/10.2118/140468-MS.

Dahi Taleghani, A., & Lorenzo, J. M. (2011, January). An alternative interpretation of microseismic events during hydraulic fracturing. In *SPE Hydraulic Fracturing Technology Conference*. Society of Petroleum Engineers.

Damani, A. (2013). Acoustic Mapping and Fractography of Laboratory Induced Hydraulic Fractures [Master's thesis]. *Norman, Oklahoma: Mewbourne School of Petroleum and Geological Engineering*.

Damani, A., Sharma, A., Sondergeld, C. et al. 2012. Acoustic emission and SEM analyses of hydraulic fractures under triaxial stress conditions. In SEG Technical Program Expanded Abstracts 2012, 1−5. Society of Exploration Geophysicists. http://dx.doi.org/10.1190/segam2012-1585.1

Dean, P., Bird, N.F., 1967. Monte Carlo estimates of critical percolation probabilities. Math. Proc. Camb. Philosophical Soc. 63 (2), 477–479.

Donahue, R. J., Clark, H. M., Atanmo, P. et al. A. J. 1972. Crack opening displacement and the rate of fatigue crack growth. International Journal of Fracture, 8(2), 209−219. https://doi.org/10.1007/BF00703882

Eisner, L., P. M. Duncan, W. M. Heigl, and W. R. Keller, 2009, Uncertainties in passive seismic monitorin: The Leading Edge, 28, no. 6, 648–655, doi:10.1190/1.31484

Elber, W. 1971. The significance of fatigue crack closure. In Damage tolerance in aircraft structures. STP 486, ASTM International, 230−242. https://doi.org/10.1520/STP486-EB

Enayatpour, S., & Patzek, T. (2013). Thermal Shock in Reservoir Rock Enhances the Hydraulic. Unconventional Resources Technology Conference (URTEC).

Erarslan, N. (2011). Static and cyclic laboratory testing of Brisbane rocks.

Erdogan, F., and Ratwani, M. 1970. Fatigue and fracture of cylindrical shells containing a circumferential crack. International Journal of Fracture Mechanics, 6(4), 379−392. https://doi.org/10.1007/BF00182626

Farahmand, B. 2001. Fracture mechanics of metals, composites, welds, and bolted joints: application of LEFM, EPFM, and FMDM theory. Boston: Kluwer Academic Publishers. https://doi.org/10.1007/978-1-4615-1585-2

Fatemi, A. (2006). Fundamentals of LEFM and applications to Fatigue Crack Growth. *Class Lecture., Department of Mechanical, Industrial and Manufacturing Engineering., University of Toledo., Ohio, USA.*

Fatt, I., 1956. The network model of porous media. I. Capillary pressure characteristics. AIME Pet. Trans. 207, 144–159.

Finney, J. L. (1970, November). Random packings and the structure of simple liquids. I. The geometry of random close packing. In *Proc. R. Soc. Lond. A* (Vol. 319, No. 1539, pp. 479-493). The Royal Society.

Forman, R. G., Keamey, V. E., and Engle, R. M. 1967. Numerical analysis of crack propagation in a cyclic-loaded structure. J. Basic Engineering. Trans ASME, 89, 459−464. https://doi.org/10.1115/1.3609637

Ge, M., 2003. Analysis of source location algorithms: Part I. Overview and non-iterative
methods. J. Acoust. Emiss. 21 (1), 21–28.

Grechka, V., P. Mazumdar, and S. A. Shapiro, 2010, Predicting permeability and gas production of hydraulically fractured tight sands from microseismic data: Geophysics, 75, no. 1, B1–B10, doi:10.1190/1.3278724.

Griffith, A. A. 1920. The phenomena of flow and rupture in solids: Phil. Trans. Roy. Soc. Lond. Ser. A, 221, 163−98. https://doi.org/10.1098/rsta.1921.0006

Guo, F., Morgenstern, N. R., & Scott, J. D. (1993, June). An experimental investigation into hydraulic fracture propagation—Part 2. Single well tests. In *International journal of rock mechanics and mining sciences & geomechanics abstracts* (Vol. 30, No. 3, pp. 189-202). Pergamon.

Haimson, B., & Fairhurst, C. (1969). Hydraulic fracturing in porous-permeable materials. *Journal of Petroleum Technology*, *21*(07), 811-817.

Haimson, B., & Fairhurst, C. (1969, January). In-situ stress determination at great depth by means of hydraulic fracturing. In *The 11th US symposium on rock mechanics (USRMS)*. American Rock Mechanics Association.

Hulse, D. S. (1959). *U.S. Patent No. 2,915,122*. Washington, DC: U.S. Patent and Trademark Office.

Inglis, C. E. 1913. Stresses in a plate due to the presence of cracks and sharp corners. Trans Naval Architect, 219−242.

Irwin, G. R. 1957. Analysis of stresses and strains near the end of a crack traversing a plate. Journal of Applied Mechanics. Vol. 24, 361−364.

Jeon, J., Bashir, M. O., Liu, J., & Wu, X. (2016, August). Fracturing Carbonate Reservoirs: Acidising Fracturing or Fracturing with Proppants?. In *SPE Asia Pacific Hydraulic Fracturing Conference*. Society of Petroleum Engineers.

Jin, X., Shah, S. N., Roegiers, J. C., & Hou, B. (2013, September). Breakdown pressure determination-a fracture mechanics approach. In *SPE Annual Technical Conference and Exhibition*. Society of Petroleum Engineers.

Jung, J., Heo, C., & Jeon, S. (2014, January). Study on Hydraulic Fracturing Evolution under Various Fluid Viscosity and Injection Rate. In *ISRM International Symposium-8th Asian Rock Mechanics Symposium*. International Society for Rock Mechanics and Rock Engineering.

Kamath, J., Xu, B., Lee, S. H., & Yortsos, Y. C. (1996, January). Pore network modeling of laboratory experiments on heterogeneous carbonates. In *SPE Annual Technical Conference and Exhibition*. Society of Petroleum Engineers.

Khishvand, M., Alizadeh, A.H., Piri, M., 2016. In-situ characterization of wettability and
pore-scale displacements during two-and three-phase flow in natural porous media. Adv. Water Resour. 97, 279–298.

Lei, X., Ma, S., 2014. Laboratory acoustic emission study for earthquake generation process. Earthq. Sci. 27 (6), 627–646.

Lockner, D., 1993. The role of acoustic emission in the study of rock fracture. Int. J. RockMech. Min. Sci. Geomechanics 30 (7), 883–899.

Mason, G., & Mellor, D. W. (1995). Simulation of drainage and imbibition in a random packing of equal spheres. *Journal of Colloid and Interface Science*, *176*(1), 214-225.

Maxwell, S., 2010, Microseismic: growth born from success: The Leading Edge, 29, no. 3, 338–343, doi:10.1190/1.3353732.

Mayerhofer, M.J., Lolon, E., Warpinski, N.R., Cipolla, C.L., Walser, D.W., Rightmire, C.M.,
2010. What is stimulated reservoir volume? SPE Prod. Operations 25 (01), 89–98.

Meek, R.A., Suliman, B., Bello, H., Hull, R., 2015. Well space modeling, SRV prediction using microseismic, seismic rock properties and structural attributes in the Eagle Ford shale of south Texas. In: Presented at SPE Unconventional Resources Technology Conference, San Antonio, Texas, USA, July 20–22. URTEC-2173501-MS.

Melrose, J. C. (1988, January 1). Interpretation Of Centrifuge Capillary Pressure Data. Society of Petrophysicists and Well-Log Analysts.

Mighani, S. (2014). Rock Tensile Failure Related Improving Hydraulic Fracture [Master’s thesis]. *Norman, Oklahoma: Mewbourne School of Petroleum and Geological Engineering*.

Moreno, C., Chitrala, Y., Sondergeld, C., & Rai, C. (2011, January). Laboratory studies of hydraulic fractures in tight sands at different applied stresses. In *2011 SEG Annual Meeting*. Society of Exploration Geophysicists.

Morita, N., Black, A. D., & Fuh, G. F. (1996, January). Borehole breakdown pressure with drilling fluids—I. Empirical results. In *International journal of rock mechanics and mining sciences & geomechanics abstracts* (Vol. 33, No. 1, pp. 39-51). Pergamon.

Mousavi, M.A., Bryant, S.L., 2012. Connectivity of pore space as a control on two-phase flow properties of tight-gas sandstones. Transp. porous media 94 (2), 1–18.

Mousavi, M.A., Bryant, S.L., 2013. Geometric models of porosity reduction by ductile grain compaction and cementation. AAPG Bull. 97 (12), 2129–2148.

Paris, P. C., Gomez, M. P., and Anderson, W. E. 1961. A rational analytic theory of fatigue. The trend in engineering, 13(1), 9−14.

Patel, S. M., Sondergeld, C. H., and Rai, C. S. 2017. Laboratory studies of hydraulic fracturing by cyclic injection. International Journal of Rock Mechanics and Mining Sciences, 95, 8−15. https://doi.org/10.1016/j.ijrmms.2017.03.008

Phillips, W.S., Fairbanks, T.D., Rutledge, J.T., Anderson, D.W., 1998. Induced microearthquake patterns and oil-producing fracture systems in the Austin chalk. Tectonophysics 289 (1), 153–169.

Prats, M. (1961, June 1). Effect of Vertical Fractures on Reservoir Behavior-Incompressible Fluid Case. Society of Petroleum Engineers. doi:10.2118/1575-G

Purcell, W.R., 1949. Capillary pressures-their measurement using mercury and the calculation of permeability therefrom. J. Petroleum Technol. 1 (02), 39–48.

Sahimi, M., 2003. In: Heterogeneous Materials: Nonlinear and Breakdown Properties and
Atomistic Modeling, vol. 2. Springer Science & Business Media.

Sahini, M., Sahimi, M., 1994. Applications of Percolation Theory. CRC Press.
Sakhaee-Pour, A., Bryant, S.L., 2015. Pore structure of shale. Fuel 143, 467–475.

Sakhaee-Pour, A. 2012. *Gas flow through shale*. PhD dissertation, The University of Texas at Austin, Austin, Texas.

Sakhaee-Pour, A., Bryant, S.L., 2014. Effect of pore structure on the producibility of tight-gas sandstones. AAPG B 98 (4), 663‒694.

Sakhaee-Pour, A., Gowhari-Anaraki, A. R., and Hardy, S. J. 2010. The effect of stiffness on stress intensity factor for a crack in annular disc under constant central torque. International Journal of Damage Mechanics, 19(8), 1001‒1015. https://doi.org/10.1177/1056789509351835

Sakhaee-Pour, A., & Bryant, S. L. (2015). Pore structure of shale. *Fuel*, *143*, 467-475.

Scholz, C.H., 1968. Microfracturing and the inelastic deformation of rock in compression. Journal of Geophysical Research 73, 1417–1432.

Shapiro, S. A., S. Rentsch, and E. Rothert, 2005, Characterization of hydraulic properties of rocks using probability of fluid-induced microearthquakes: Geophysics, 70, no. 2, F27–F34, doi:10.1190/1.1897030.

Shapiro, S. A., E. Rothert, V. Rath, and J. Rindschwentner, 2002, Characterization of fluid transport properties of reservoirs using induced microseismicity: Geophysics, 67, 212–220, doi:10.1190/1.1451597

Shigley, J. E., Mischke, C. R., and Budynas, R. G. 2004. Mechanical engineering design. New York: McGraw-Hill.

Sil, S., D. Lane, and J. Gabler, 2014, Permeability prediction using pressure and microseismic data: a laboratory experiment: Society of Exploration Geophysicists, SEG 2014 Annual Meeting, p. 2299-2303.

Stein, S., Wysession, M., Houston, H., 2003. Books-an introduction to seismology, earthquakes, and earth structure. Phys. Today 56 (10), 65–72.
Stephens, R. I., Fatemi, A., Stephens, R. R., Fuchs, H. O. 2000. Metal fatigue in engineering. New York: John Wiley & Sons.

Stephens, R. I., Fatemi, A., Stephens, R. R., et al. 2000. Metal fatigue in engineering. New York: John Wiley & Sons.

Tarrahi, M., Jafarpour, B., Ghassemi, A., 2015. Integration of microseismic monitoring data into coupled flow and geomechanical models with ensemble Kalman filter. Water Resour. Res. 51 (7), 5177–5197.

Warpinski, N.R. 2010. Source-mechanism studies on microseismicity induced by hydraulic fracturing, SPE 135254 presented at SPE Annual Technical Conference and Exhibition, Florence, Italy.

Washburn, E.W., 1921. The dynamics of capillary flow. Phys. Rev. 17 (3), 273.

Yapar, O., Basu, P.K., Volgyesi, P., Ledeczi, A., 2015. Structural health monitoring of bridges with piezoelectric AE sensors. Eng. Fail. Anal. 56, 150–169.

Zang, A., Stephansson, O., & Zimmermann, G. (2017). Keynote: Fatigue Hydraulic Fracturing. *Procedia engineering*, *191*, 1126-1134.

Zang, A., Wagner, F.C., Stanchits, S., Janssen, C., Dresen, G., 2000. Fracture process zone in granite. J. Geophys. Res. Solid Earth 105 (B10), 23651–23661.

Zang, A., Yoon, J. S., Stephansson, O., & Heidbach, O. (2013). Fatigue hydraulic fracturing by cyclic reservoir treatment enhances permeability and reduces induced seismicity. *Geophysical Journal International*, *195*(2), 1282-1287.

Appendix

The appendix contains 2 full length papers (1) Journal paper published in Journal of Petroleum Science and Engineering, ‘Integrating acoustic emission into percolation theory to predict permeability enhancement’ (2) Conference paper presented at Unconventional Resources Technology Conference (URTeC), ‘Effects of Cycling fracturing on Acoustic Events and Breakdown pressures’

Journal of Petroleum Science and Engineering 160 (2018) 152–159

Contents lists available at ScienceDirect

Journal of Petroleum Science and Engineering

journal homepage: www.elsevier.com/locate/petrol

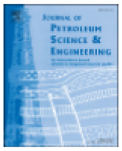

Integrating acoustic emission into percolation theory to predict permeability enhancement

A. Sakhaee-Pour [a,*], Abhishek Agrawal [b]

[a] Department of Petroleum Engineering, University of Houston, Houston, TX, USA
[b] Petroleum and Geological Engineering School, University of Oklahoma, OK, USA

ARTICLE INFO

Keywords:
Acoustic emission (AE)
Percolation theory
Hydraulic fracturing

ABSTRACT

Hydraulic fracturing allows us to enhance the transport properties of a tight formation, but it remains difficult to predict the enhancement as a function of recorded acoustic events. With this in mind, we initiate pore-scale modeling of acoustic emission (AE) events based on percolation theory. The main objective is to predict the permeability enhancement by accounting for the number of AE events. We first develop a physically representative model of the intact pore space of the matrix of Tennessee sandstone at the core scale based on petrophysical measurements, which are porosity, permeability, and capillary pressure. A block-scale sample of the formation is then hydraulically fractured, where piezoelectric sensors record the events generated during stimulation. We predict the permeability enhancement of the formation at the core scale by accounting for the number of AE events per unit volume. Independent petrophysical measurements corroborate the predicted results based on percolation theory. The proposed model has major implications for characterizing the transport properties of the stimulated reservoir volume.

1. Introduction

An acoustic emission (AE) is a transient elastic wave generated by the rapid release of energy within a material (Lockner, 1993), which can be detected using seismometers. AE events are associated with brittle fractures due to pressure and temperature. Analyzing AE has applications in earthquake seismology (Lei and Ma, 2014), predicting rock bursts and mine failures, fracture mapping (Phillips et al., 1998), monitoring mechanical performance (Chong et al., 2003), monitoring the condition of tools and health monitoring (Yapar et al., 2015).

AE takes different forms because of variations in the frequency and amplitude of waves. Both seismic and microseismic events—a physical concept in earthquake seismology—are derived from AE. The science of seismology's study of earthquake activity and the geophysical study of microseismic activity in rock are similar. There is a generation of acoustic signals whenever irreversible damage occurs (Lockner, 1993). The acoustic signals provide information about the size, the location, and the deformation mechanisms.

Under loading, the structure deteriorates progressively in rocks and concrete, first in an uncorrelated way reflecting intrinsic heterogeneities. The stress fields of the microcracks interact, and the microcracks become correlated, as the density of the microcracks increases. The microcracks may coalesce to form a connected-through fracture as the culmination of progressive damage. AE events, due to microcracks growth, precede the macroscopic failure of rock and concrete samples under constant stress or constant strain rate loading (Stein et al., 2003; Ge, 2003).

The petroleum industry carries out hydraulic fracturing in tight sand and shale reservoirs to improve their transport properties. A better approximation of the location and size of the connected fractures is crucial for evaluating success of formation stimulation and for modeling reservoir performance. The fracture orientation is also important in terms of stimulating the reservoir efficiently with minimum interference.

Fractures created during stimulation can form a complex pattern, and are not necessarily planar. Thus, researchers have introduced the stimulated rock volume (SRV) for estimating well performance (Mayerhofer et al., 2010) based on three-dimensional microseismic events. A recent study has proposed using microseismic density to compute SRV at the reservoir scale (Meek et al., 2015), where gridblocks with no events are unstimulated and have intact transport properties. The transport properties of gridblocks with AE events are increased using an ad-hoc model. Researchers have also used a Kalman filter to interpolate the transport properties at the reservoir scale (Tarrahi et al., 2015). The proposed models have had some success in predicting the production rate of a formation, but they have not been tested against core- or block-scale

---

[*] Corresponding author.
E-mail address: asakhaee@central.uh.edu (A. Sakhaee-Pour).

https://doi.org/10.1016/j.petrol.2017.10.003
Received 4 January 2017; Received in revised form 21 July 2017; Accepted 2 October 2017

measurements. The validity of the proposed models is critical, considering that reservoirs are highly heterogeneous, and the effective transport properties are controlled by different physics at different scales.

Researchers also analyzed the fracture propagation based on percolation theory. Sahimi (2003) suggested that the initial stages of brittle fractures and percolation processes in a lattice are more or less similar. He proposed that percolation is a static process in which failure has nothing to do with the stress and strain field in the lattice, whereas the growth of fractures is not random, and depends on the stress and strain in the solid. Under certain conditions, Sahimi (2003) contended, the accumulation of damage and growth of cracks occur at random—for example, in a natural rock, where heterogeneities are broadly distributed and percolation systems can describe fracture.

Sahimi (2003) also stated that, in the initial stages, the bonds that break are random, and the stress enhancement at the tip of a given microcrack is not large enough to ensure that the next microcrack occurs at the tip of the first microcrack. As more microcracks nucleate, however, the effect of stress enhancement becomes stronger, and deviations from random percolation increases. We assume that our lab measurements qualify for this condition, and use percolation theory to predict the permeability enhancement.

The present study analyzes the permeability enhancement of Tennessee sandstone via analyzing AE events. It develops a physically representative model for the pore space at the core scale, which embraces pore throats and pore bodies. It then uses percolation theory to predict the permeability change at the core scale. The predicted results are tested against lab measurements.

2. Methodology

2.1. Pore-scale modeling

Pore-scale modeling is concerned with developing a physically representative model of the pore space of a formation. The pore space is composed of pore bodies and pore throats. The pore throats are narrow regions of the pore space that govern the interactions between connected pore bodies. The topological parameters of the pore throats and their spatial distribution control the effective transport properties of the matrix of a formation.

There are two common methods for deriving the connected network of the pore throats and pore bodies: non-theoretical and theoretical. The non-theoretical models are based on extracting the network from micro-CT images of a sample (Khishvand et al., 2016) without any prior assumptions about the pore topology. The theoretical models use a theoretical distribution of the connected network of the pore throats and bodies to study the transport properties at the core scale.

Washburn (1921) proposed the first theoretical pore model by representing the pore space as an assemblage of cylindrical capillaries. Purcell (1949) extended that concept to predict the permeability from capillary pressure measurements. Subsequently, Fatt (1956) suggested that the pore space could be mimicked using a regular lattice. Another theoretical approach assumes that spheres can represent the grains of a sedimentary rock, and thus the empty spaces between them mimic the void space of the porous medium (Bryant et al., 1993). More recently, researchers have shown that the acyclic pore model has applications in capturing the transport properties of shale formations (Sakhaee-Pour and Bryant, 2015) and those of The Geysers. Another example of a theoretical pore model is the multi-type model, which can be used for tight gas sandstones.

The trend of capillary pressure measurements with wetting-phase saturation depends on the spatial distribution of the pore-throat size in the network of the connected pores (Mousavi and Bryant, 2012, 2013). We often inject mercury, which is a nonwetting phase to the solid grains, into the rock sample to measure the capillary pressure. Fig. 1a shows two common trends of the capillary pressure with wetting phase saturation: non-plateau-like and plateau-like (Sakhaee-Pour and Bryant, 2015).

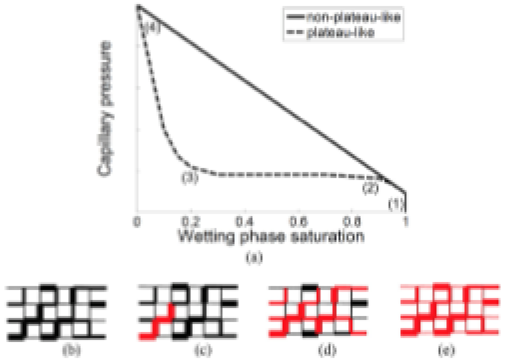

Fig. 1. (a) The plateau-like and non-plateau-like trends of capillary pressure with wetting phase saturation. (b–e) The mercury intrusion experiments with the plateau-like trend, which corresponds to the random distribution of the pore-throat size on the network of connected pores. The mercury is shown in red and the line thickness is representative of the pore-throat size. (For interpretation of the references to colour in this figure legend, the reader is referred to the web version of this article.)

The nonwetting phase can invade a pore only when its capillary pressure is larger than the entry pressure of the corresponding pore throat. Wider pore throats have lower resistance against the invasion. In the network of the connected pores, the nonwetting phase can invade a pore only if it has access to the corresponding pore-throat size whose entry pressure is not larger than the applied capillary pressure. Thus, the invasion of the pore space is delayed, which is relevant to the plateau-like trend, when the spatial distribution of the pore-throat size is random. Fig. 1b–e shows how the random spatial distribution of the pore-throat size leads to a plateau-like trend in capillary pressure measurements, where the red represents the nonwetting phase and the line thickness denotes the pore throat size.

2.2. A physically representative model of Tennessee sandstone

We analyzed Tennessee sandstone, which is homogeneous and light brown in color. Routine core analysis showed that the porosity and the permeability of an intact Tennessee core plug were equal to 5.5% and 4 μd. Mineralogy was performed using the Fourier Transform Infrared Spectroscopy (FTIR) technique, and quartz was found to be the main mineral (average 59 wt %) lesser minor amounts of clays. An average grain size of 190 μm was obtained from a thin-section image of Tennessee sandstone taken under polarized light.

Mercury injection allowed us to determine the pore-throat size distributions. Fig. 2 shows the lab measurements conducted on a core plug. Our conclusion is that the pore-throat size distribution in the network of the connected pores is random because the trend of the capillary pressure with wetting-phase saturation is plateau-like. The trend of the capillary pressure with non-wetting phase saturation (= 1–wetting-phase saturation) is also plateau-like, but we illustrate the former one as it is more common.

The pore-throat size distribution is determined using the capillary pressure measurements (Fig. 2b). The capillary pressure is increased incrementally, and the injected fluid volume at each increment is measured. The incremental volume indicates the pore volume associated with a specific pore-throat size, which is determined from the applied capillary pressure. The volume fraction of each pore-throat size is equal to the ratio of the injected mercury volume to the pore volume, and the pore-throat size is a function of the capillary pressure, based on the Young-Laplace relation, as follows:

percolation theory based on the random distribution assumption. It then clarifies how percolation theory can relate AE events to the high-permeability paths created in formation stimulation.

Percolation takes place when one medium spreads randomly through another (Berkowitz and Ewing, 1998). Examples include the diffusion of a solute through a solvent, disease spreading in a society, and fluid spreading in a porous medium (Broadbent and Hammersley, 1957). Randomness is the key feature of percolation theory and arises due to different mechanisms that are relevant to the penetrating and penetrated media (Sahini and Sahimi, 1994).

Site and bond percolations are the two main categories of percolation phenomena. The former is more relevant to the present study and discussed here. Fig. 3a shows a network model where the black circles and the dashed lines indicate the absence of the fluid. The red squares and the solid lines indicate the presence of the fluid. The percolation takes place when the fluid forms a connected-through path in the model. The connected-through path is shown in red in Fig. 3b.

The number of the sites occupied by the fluid relative to the total number of sites is equal to the probability (p), which is equal to unity when the fluid fills all the sites and to zero when there is no fluid in the model. The probability of the model is equal to the percolation threshold when percolation takes place (Dean and Bird, 1967). The number of the occupied sites exceeds a certain number when the probability becomes equal to the percolation threshold. Fig. 3c shows a network model where the fluid occupies different sites randomly, and the percolated path is shown in red in Fig. 3b where the fluid forms a path from the left to the right of the model.

We use a physically representative pore model to implement the effects of the microfractures on the transport properties. The pore space is treated as a network of pore bodies (sites) that interact with each other through pore throats (Fig. 3c). Each event in the representative volume is indicative of a large pore body, shown as a red triangle in Fig. 3c. The large pore body, whose volume is equal to the void space that resides in the microfracture, is connected to adjacent pores via pore throats, shown with dashed red lines. The transport properties of the pore throats connected to the large pore are dependent on the characteristic size of the microfracture.

The large pore body is distributed randomly as a site, which classifies the problem as a site percolation. Percolation theory predicts large-scale behavior by accounting for randomly interconnecting small-scale phenomena. Our assumption is that the small-scale fractures form a connected-through path when the number of AE events per unit volume exceeds a certain value, which is relevant to the percolation threshold.

The large pores (red triangles in Fig. 3c) are connected to all the pores of the intact pore space (black circles in Fig. 3c) in the stimulated region. Fig. 3 is a conceptual illustration, and the permeability calculation based on the proposed method is discussed subsequently (Eq. (3)). The volume fraction of the stimulated regions depends on the number of AE events per unit volume of the representative volume that corresponds to the percolation threshold. For instance, Fig. 3c shows a condition where the number of AE events per unit volume of the representative volume is equal to 2, and the large pores form a connected-through path when this ratio becomes equal to 6.

The total volume of the physically representative model is divided into the number of events recorded per unit volume for the fractured plug. The volume fraction of the stimulated region for partially fractured samples is equal to the ratio of its number of events per unit volume to the number of events per unit volume for the fractured plug. We consider a one-dimensional flow model where the stimulated and intact regions act in series, which allows us to determine the core-plug permeability as follows:

$$K_{eff} = \frac{N}{\frac{n}{K_f} + \frac{N-n}{K_m}} \tag{3}$$

where K_{eff} is the effective permeability of a partially fractured plug, K_m is the matrix permeability of an intact sample, K_f is the permeability of a fully fractured plug, N is the total volume of the model, and n is the stimulated region volume.

2.4. *Hydraulic fracturing of a Tennessee sandstone block*

We cut and polished a cylindrical Tennessee sandstone and stimulated the block-scale sample under triaxial loading conditions. The sample diameter was 4 in and its length was approximately 5–1/2 in. A hole of ¼ inch in diameter was drilled in the center of the core and extended up to half the sample length. The hole was completed with a ⅛ inch OD tube that was cemented (Damani, 2013).

Triaxial stress (vertical stress = 3000 psi, maximum horizontal stress = 2000 psi, minimum horizontal stress = 500 psi) was applied to replicate the in-situ stress conditions. The loading system was designed to allow triaxial loading of the rock sample with simultaneous injection of fracturing fluid and recording of acoustic emissions. The three stresses were applied using confining fluid pressure, hydraulic flat jacks, and an axial piston (Fig. 4).

Oil was then injected into the hole at a rate of 10 cm^3/min. The pressure starts to increase in the hole and the fluid diffuses into the pore space of the rock. Consequently, localized microcracking is initiated in the rock and with continued oil injection, the microcracks start to coalesce and form a large fracture. The block breaks down at 4336 psi, which was indicated by a sharp fall in the pump pressure.

The AE events can be divided into pre- and post-breakdown events. Pre-breakdown events may be caused by rock failure due to stress induced by wellbore pressurization and the injected fluid diffusing locally into matrix whereas post-breakdown events may be caused by flow through the fracture and failure of asperities along the fracture faces. In our experiment, most events were post-breakdown events (Fig. 5).

There were 16 piezoelectric sensors mounted on the block, with one on the top, one on the bottom, and the remaining 14 on the cylindrical surface of the sample, distributed uniformly over the azimuth and the height. AE events showed a delayed response, with the first events being captured at the breakdown and thereafter increasing rapidly. The average error in hypocenter locations for this test was+/-5.34 mm, and the amplitude of the events ranged from 0.1 to 0.9 V. The total number of events was equal to 1564, and the density was higher close to the large fracture (Fig. 6). To locate the AE events, the individual arrival times of the compressional waves associated were recorded automatically. The first arrivals were used to determine the event location using a weighted least squares inversion algorithm (Damani, 2013). A frequency of 50 kHz to 1.5 MHz was used to filter the good events; the rest of the events with frequencies outside the range were treated as noise.

3. Results

The physically representative pore model is used here to predict the permeability enhancement at the core scale. The number of AE events per unit volume (#Events/volume) is determined for a core plug that has a large fracture, which can be observed with the naked eye. This ratio corresponds to the percolation ratio when the fracture forms a connected-through path. The permeability measurements of other core plugs, extracted from the stimulated block, provide independent evidence to test the model.

We extracted five core plugs from the stimulated Tennessee sandstone block for petrophysical characterization (Fig. 7). One plug was extracted right on top of the large fracture (Left wing in Fig. 7a), whereas the other four plugs were extracted from either side of the large fracture (Right Wing in Fig. 7a). Table 1 lists the spatial locations of the core plugs with respect to the coordinate system shown in Fig. 7, their bulk volume, and the number of AE events. The core plug with the connected-through fracture is referred to as the Fractured plug in Table 1 and has the largest #Events/volume and highest permeability; the other plugs are

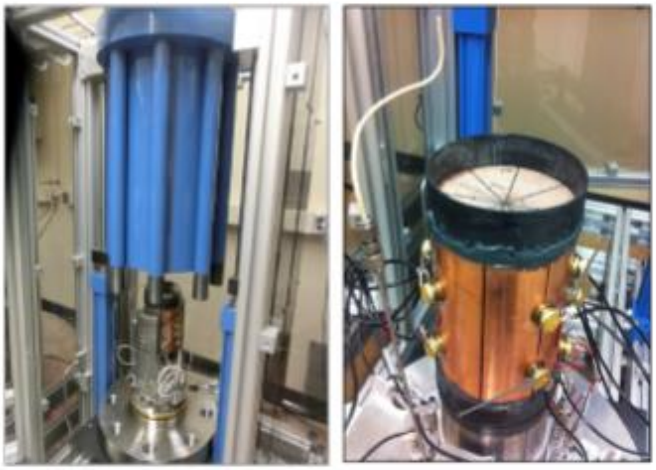

Fig. 4. Hydraulic fracturing lab experimental setup. The figure on the left shows an expanded view of the triaxial loading system with axial loading, confining vessel and flat jacks to apply transverse stress. The figure on the right shows the sample covered with copper jacket mounted on the base plate of the triaxial loading system. (Damani et al., 2012; Damani, 2013).

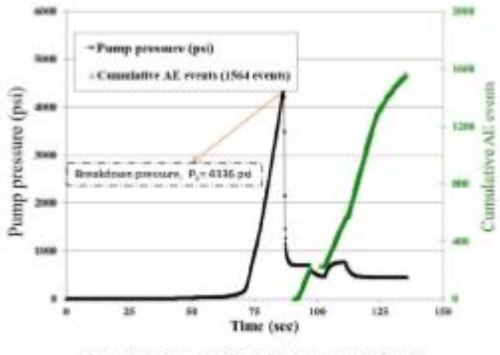

Fig. 5. Pump pressure and cumulative AE events with time.

named Plugs 1–4 in Table 1.

Fig. 7 shows a scanning electron microscope (SEM) image of the formation where there is a connected-through fracture in the sample, which is created during hydraulic fracturing of the block. The high-resolution image shows the fracture with no confinement. The high resolution suggests that the aperture size of the connected fracture could be on the order of 1–10 μm.

We measured the permeability of each core plug listed in as a function of effective stress (Table 2). The confining stress was changed where the pore pressure was 200 psi. The pore pressure was fixed using the AP-608™ permeameter, and the effective stress was calculated as follows:

$$\text{Effective stress} = \text{Confining stress} - \text{Pore pressure} \tag{4}$$

The lab measurements are normalized with respect to the measured value measured for each sample when the effective stress is equal to 300 psi (Fig. 8). The results are normalized with respect to the confined conditions because they are more representative of in-situ conditions. The rate of the permeability decrease with the effective stress is relatively similar for different samples, especially at low effective stress. The similarity suggests that the permeability decline is controlled by the change in the effective aperture size of the fractures. The similarity could also be a result of a homogeneous material distribution. The decrease rate of the fractured plug deviates from the other plugs as the effective stress increases, which could be due to the plastic deformation. The lab measurements revealed that the plug permeability did not recover fully to the original value because of the plastic deformation after the test when the confining stress was removed.

The fractured plug permeability was also measured as a function of the confining stress. The fractured plug permeability was 5.342 md when the confining stress was equal to 1000 psi. The measured permeability is used as an estimate for the permeability of the stimulated region (Fig. 3c). The measured permeability is also used to normalize the results, denoted by $k_{\text{fractured plug}}$ in Fig. 8.

The spatial locations of the recorded events and the bulk volume of each core plug determine the number of AE events per unit volume (#Events/volume). This ratio is equal to 6.95 cm^{-3} for the fractured plug, which corresponds to the percolation threshold. We predicted the permeability of the core plug when this ratio is smaller than the percolation threshold based on percolation theory, using the physically representative pore model. Fig. 9 reveals that the core-scale measurements corroborate the predicted results. The permeability of the formation remains close to the intact value at the core scale when the #Events/volume is smaller than the threshold value. Our model also suggests that the stimulated permeability increases by a factor of 2 relative to the intact permeability (~ 4md). Thus, the intact permeability remains close to the matrix permeability, as opposed to the fractured plug permeability.

We used all the data available from the core plugs recovered from the block sample to test our model. Most AE events occur on the fracture, which is the reason for the absence of lab measurements with #Event/volume between 3 and 6. The core plugs with small #Events/volume were taken as close as possible to the main fracture. Nonetheless, the simulation results and lab measurements indicate that the permeability close to the main fracture remains close to the intact permeability and the enhanced permeability does not increase linearly with #Events/volume.

Now, we turn to the sensitivity of the results to the amplitude of the events recorded (Fig. 10). The amplitude cutoff (%) is defined as removing events that have amplitude values in the bottom x% of the total events. The number of events per unit volume (#Events/volume) decreases the most for the fractured plug. The significant decrease for the

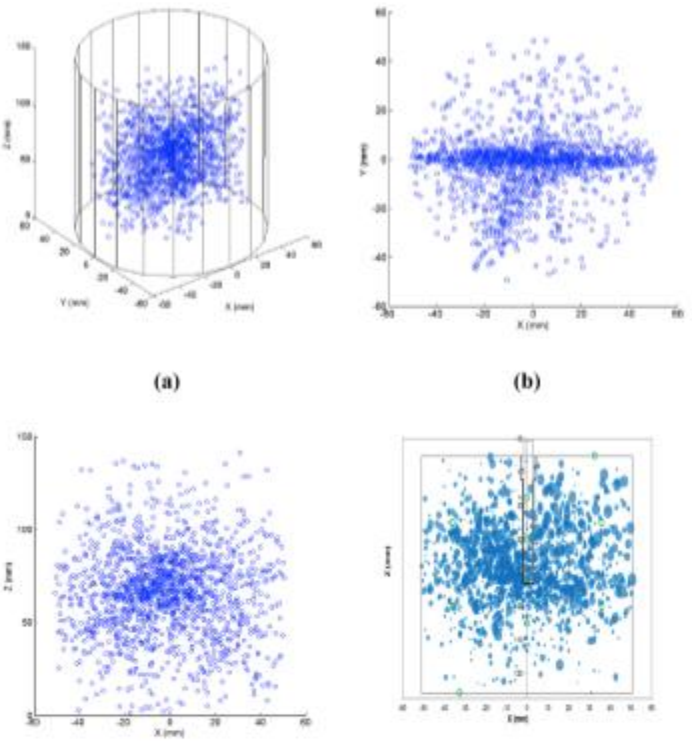

(a) (b)

(c) (d)

Fig. 6. Spatial locations of 1564 AE events recorded during hydraulic fracturing of a Tennessee sandstone block in a (a) three-dimensional coordinate system, (b) X-Y plane, and (c) X-Z plane. (d) The size of the blue bubbles corresponds to the amplitude of the AE events. The green circles represent the sensor locations. (For interpretation of the references to colour in this figure legend, the reader is referred to the web version of this article.)

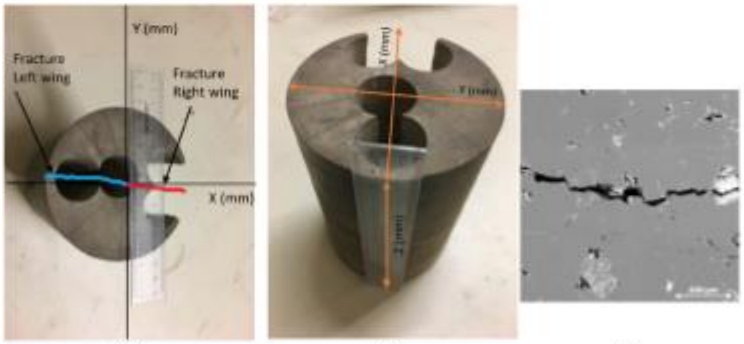

(a) (b) (c)

Fig. 7. (a-b) Block-scale sample of a hydraulically fractured Tennessee sandstone, where the holes show the locations of the extracted core plugs for permeability measurements. The fracture left and right wings are shown by blue red lines, respectively. (c) Scanning electron microscope (SEM) image of the fractured core plugs that shows a connected-through fractures in the sample. (For interpretation of the references to colour in this figure legend, the reader is referred to the web version of this article.)

Table 1
Spatial location, number of AE events, and the block volume of the core plug extracted from the stimulated Tennessee sandstone block shown in Fig. 7.

Plug	X(mm)	Y(mm)	Z(mm)	#Events	Bulk volume (cm^3)	#Events/ volume (cm^{-3})
Plug 1	30	12.5	31	2	15.21	0.13
Plug 2	30	12.5	58	12	15.21	0.79
Plug 3	30	−12.5	31	6	13.25	0.45
Plug 4	30	−12.5	58	21	13.25	1.54
Fractured plug	−32	0	78	134	19.27	6.95

Table 2
Plug length, diameter, and permeability at 300 psi effective stress.

	Length (mm)	Diameter (mm)	Permeability (md)
Plug 1	31	25.4	0.008
Plug 2	27	25.4	0.007
Plug 3	31	25.4	0.007
Plug 4	27	25.4	0.007
Fractured plug	39	25.4	8.097

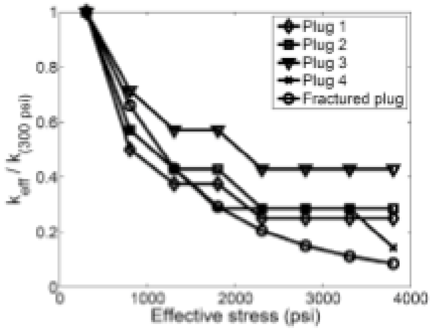

Fig. 8. The permeability decreases as the effective stress increases for different plugs.

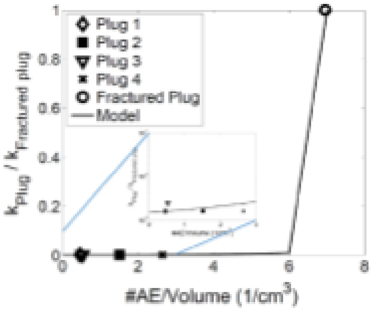

Fig. 9. Core-scale measurements corroborate the physically representative pore model, which predicts the permeability enhancement based on percolation theory. The stimulated permeability remains very close to that of the matrix, as opposed to that of the fractured plug, when the number of AE events per unit volume (#Events/volume) is smaller than the percolation threshold.

fractured plug indicates that there is a wide amplitude range. Nevertheless, it is apparent that the cutoff value does not change the trend of results because it only shifts them monotonically.

Dahi Taleghani and Lorenzo (2011) indicated that low-frequency events were the tensile events causing Mode I failure. Low-frequency events are beyond the scope of the present work, because our device does not record events below 50 kHz. We considered four kinds of failure mechanisms: shear, tensile, compressive, and complex. Our hypothesis is that each event is an indicative of a microfracture, and the microfractures form a macrofracture when #Events/volume reaches a critical value.

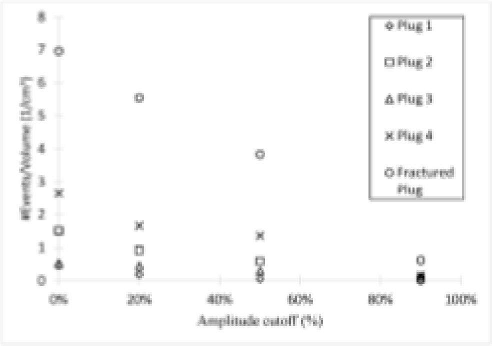

Fig. 10. #Events/volume decreases monotonically with increasing amplitude cutoff.

4. Discussion

In petroleum engineering, the ultimate goal of most research, including the present study, is to be applied in field. The presented model and lab measurements predict the permeability enhancement of a stimulated region, without a connected-through fracture, based on its acoustic emission. The stimulated region is also referred to as the process zone (Zang et al., 2000). Our study suggests that the enhanced permeability remains close to the intact permeability, and that it is unrealistic to use a linear approximation for the stimulated region permeability. Knowing that, in the absence of a connected-through fracture, the permeability increase is not very significant is crucial for building a realistic reservoir model.

Another issue is the size of the stimulated region. The size of the stimulated region, whose permeability is close to the intact permeability, relative to the overall domain is equal to the size of the core plug to the block. We can predict the stimulated region size if the results can be scaled to the field conditions. The stimulated region size close to each fracture can be predicted by accounting for the fracture length.

The presented results are relevant to fluid injection into a dry sample. The size of the stimulated region and the spatial distribution of the events may change if the sample is initially saturated and when conducted for a different formation. Our model is based on the assumption that the spatial distribution of the pore-throat size is random, which is realistic for Tennessee sandstone. The developed model needs modifications when this assumption is not realistic.

5. Conclusions

We developed a physically representative pore model of an intact Tennessee sandstone at the core scale by analyzing its permeability, porosity, and capillary pressure measurements. Our main objective was to predict the permeability enhancement by accounting for acoustic emission (AE) events. Our assumption was that each event is represen~~tative of a microcrack or is indicative of an asperity which compressed~~ during fracture closure. This assumption implies that a connected-through fracture is formed when the number of AE events per unit volume becomes larger than the threshold value.

We predicted the permeability enhancement of a formation based on percolation theory. Our study shows that the stimulated permeability of a formation at the core scale is much smaller than the fractured plug permeability if the number of events per volume is smaller than the threshold value. The permeability enhancement of the core plug, relative to intact conditions, is close to 2 when the fracture does not form a connected-through path. The proposed model, which relates the number of acoustic emission events to the enhanced permeability based on percolation theory, has major applications in determining the transport properties of the stimulated reservoir volume.

Declarations

The authors declare that they have no competing interests. ASP developed and tested the main concept of the present study. He integrated the acoustic emission events into percolation theory to predict the permeability enhancement. ASP wrote and revised the manuscript. AA coded the two-dimensional network of the sample and prepared the plots.

Acknowledgements

The authors are grateful to Carl Sondergeld and Akash Damani for sharing some of the lab measurements (Damani et al., 2012; Damani 2013) analyzed in this study. The authors are also grateful for the constructive comments of four anonymous reviewers.

References

Berkowitz, B., Ewing, R.P., 1998. Percolation theory and network modeling applications in soil physics. Surv. Geophys. 19 (1), 23–72.
Broadbent, S.R., Hammersley, J.M., 1957. Percolation processes. Math. Proc. Camb. Philosophical Soc. 53, 629–641.
Bryant, S.L., Mellor, D.W., Cade, C.A., 1993. Physically representative network models of transport in porous media. AIChE J. 39 (3), 387–396.
Chong, K.P., Carino, N.J., Washer, G., 2003. Health monitoring of civil infrastructures. Smart Mater. Struct. 12 (3), 483.
Dahi Taleghani, A., Lorenzo, J.M., 2011, January 1. An Alternative Interpretation of Microseismic Events during Hydraulic Fracturing. Society of Petroleum Engineers. https://doi.org/10.2118/140468-MS.
Damani, A., Sharma, A., Sondergeld, C., Rai, C.S., 2012. Acoustic emission and SEM analyses of hydraulic fractures under triaxial stress conditions. In: Presented at SEG Annual Meeting, Las Vegas, Nevada, USA, November 4–9. SEG-1585.
Damani, A., 2013. Acoustic Mapping and Fractography of Laboratory Induced Hydraulic Fractures (Doctoral dissertation, University of Oklahoma).
Dean, P., Bird, N.F., 1967. Monte Carlo estimates of critical percolation probabilities. Math. Proc. Camb. Philosophical Soc. 63 (2), 477–479.
Fatt, I., 1956. The network model of porous media. I. Capillary pressure characteristics. AIME Pet. Trans. 207, 144–159.
Ge, M., 2003. Analysis of source location algorithms: Part I. Overview and non-iterative methods. J. Acoust. Emiss. 21 (1), 21–28.
Khishvand, M., Alizadeh, A.H., Piri, M., 2016. In-situ characterization of wettability and pore-scale displacements during two-and three-phase flow in natural porous media. Adv. Water Resour. 97, 279–298.
Lei, X., Ma, S., 2014. Laboratory acoustic emission study for earthquake generation process. Earthq. Sci. 27 (6), 627–646.
Lockner, D., 1993. The role of acoustic emission in the study of rock fracture. Int. J. Rock Mech. Min. Sci. Geomechanics 30 (7), 883–899.
Mayerhofer, M.J., Lolon, E., Warpinski, N.R., Cipolla, C.L., Walser, D.W., Rightmire, C.M., 2010. What is stimulated reservoir volume? SPE Prod. Operations 25 (01), 89–98.
Meek, R.A., Suliman, B., Bello, H., Hull, R., 2015. Well space modeling, SRV prediction using microseismic, seismic rock properties and structural attributes in the Eagle Ford shale of south Texas. In: Presented at SPE Unconventional Resources Technology Conference, San Antonio, Texas, USA, July 20–22. URTEC-2173501-MS.
Mousavi, M.A., Bryant, S.L., 2012. Connectivity of pore space as a control on two-phase flow properties of tight-gas sandstones. Transp. porous media 94 (2), 1–18.
Mousavi, M.A., Bryant, S.L., 2013. Geometric models of porosity reduction by ductile grain compaction and cementation. AAPG Bull. 97 (12), 2129–2148.
Phillips, W.S., Fairbanks, T.D., Rutledge, J.T., Anderson, D.W., 1998. Induced microearthquake patterns and oil-producing fracture systems in the Austin chalk. Tectonophysics 289 (1), 153–169.
Purcell, W.R., 1949. Capillary pressures-their measurement using mercury and the calculation of permeability therefrom. J. Petroleum Technol. 1 (02), 39–48.
Sahimi, M., 2003. In: Heterogeneous Materials: Nonlinear and Breakdown Properties and Atomistic Modeling, vol. 2. Springer Science & Business Media.
Sahini, M., Sahimi, M., 1994. Applications of Percolation Theory. CRC Press.
Sakhaee-Pour, A., Bryant, S.L., 2015. Pore structure of shale. Fuel 143, 467–475.
Stein, S., Wysession, M., Houston, H., 2003. Books-an introduction to seismology, earthquakes, and earth structure. Phys. Today 56 (10), 65–72.
Tarrahi, M., Jafarpour, B., Ghassemi, A., 2015. Integration of microseismic monitoring data into coupled flow and geomechanical models with ensemble Kalman filter. Water Resour. Res. 51 (7), 5177–5197.
Washburn, E.W., 1921. The dynamics of capillary flow. Phys. Rev. 17 (3), 273.
Yapar, O., Basu, P.K., Volgyesi, P., Ledeczi, A., 2015. Structural health monitoring of bridges with piezoelectric AE sensors. Eng. Fail. Anal. 56, 150–169.
Zang, A., Wagner, F.C., Stanchits, S., Janssen, C., Dresen, G., 2000. Fracture process zone in granite. J. Geophys. Res. Solid Earth 105 (B10), 23651–23661.

URTeC: 2669677

Effects of Cyclic Fracturing on Acoustic Events and Breakdown Pressure

Abhishek Agrawal, A. Sakhaee-Pour, The University of Oklahoma, USA.

DOI 10.15530/urtec-2017-2669677

This paper was prepared for presentation at the Unconventional Resources Technology Conference held in Austin, Texas, USA, 24-26 July 2017.

Abstract

In hydraulic fracturing, large volumes of fluid and sand are injected into the formation to enhance the transport properties. In conventional fracturing, the fluid pressure is increased monotonically to reach failure in a single cycle. The maximum pressure for the failure can be reduced if we increase and decrease the fluid pressure cyclically (cyclic fracturing). More acoustic events, which correspond to a larger enhancement in the stimulated region's permeability, are recorded in cyclic fracturing. In the present study, we discuss the difference between the recorded events for the two methods. Four blocks of Tennessee sandstone were hydraulically fractured under triaxial stress: two under conventional loading and two under cyclic loading. We also use a modified Paris law to predict the breakdown pressure in cyclic fracturing, based on linear elastic fracture mechanics (LEFM), which treats the solid domain as an isotropic and linear elastic medium. We use the two conventional tests and one cyclic test to determine the unknown parameters in the modified Paris law. The tuned model, with determined parameters, can help us design an optimum scenario that is fundamentally different from the conventional method for formation stimulation. The results are promising and more lab measurements are required to test the accuracy of the developed model.

Introduction

Hydraulic fracturing has become an essential part of the petroleum industry, as it enables us to produce hydrocarbon from tight formations by improving their transport properties. Most of the existing techniques are based on linear elastic fracture mechanics (LEFM); thus, that topic is briefly reviewed here.

Inglis (1913) started linear elastic fracture mechanics (LEFM) by analyzing the stress field around an elliptical crack in brittle materials. He proposed that the stress at the crack tip is proportional to the length of the major axis of the crack and the tensile load. Later, Griffith (1920) used the energy balance criterion to derive a relation for crack propagation. Irwin (1957) described the stress at the crack tip in terms of the stress intensity factor (SIF).

Cyclic loading, or fatigue (Shigley et al. 2004), is the application of fluctuating stresses or strains. It has many applications in other engineering fields, such mechanical and aerospace engineering, examples of which include automobile axles, wheels, cranes, and various aircraft parts. The cyclic loading is often classified into high cycle and low cycle. High-cycle fatigue (HCF) is a cyclic loading where the sample has a relatively long life (10^4–10^8 cycles). Low-cycle fatigue, on the other hand, corresponds to large loading with a fairly short life (< 10^4 cycles).

The life of the sample is often predicted based on various versions of Paris law (Paris et al. 1961), which is an empirical correlation. It predicts the crack growth per each cycle. The sample fails when its stress intensity factor reaches a critical value. The original Paris law appeared in 1961 and was improved over the years (Forman et al. 1967; Erdogan and Ratwani 1970; Elber 1971; Donahue et al. 1972).

In petroleum engineering, we usually increase the fluid pressure monotonically until the formation or rock sample fails. This is a conventional fracturing (a single cycle). In the present study, we model rock failure under cyclic loading based on a modified Paris law. We first determine the unknown parameters of the model based on cyclic fracturing for one sample. We then predict the breakdown pressure and the number of cycles required for another sample using the tuned model. The results of the modified Paris law are promising.

Linear Elastic Fracture Mechanics (LEFM)

In linear elastic fracture mechanics (LEFM), we assume that the solid medium is an isotropic and linearly elastic continuum (Stephens et al. 2000). LEFM has many applications because it simplifies the complex behavior of a solid medium. It provides a reliable solution when the rock's behavior shows that it is brittle. Under these conditions, the stress intensity factor (SIF) can be used to estimate the stress state near the crack tip as follows (Sakhaee-Pour et al. 2010):

$$K = Y\sigma_e\sqrt{\pi a} \quad \sigma_e = P_p - \sigma_c \tag{1}$$

where K is the stress intensity factor, a is the crack length, Y is the geometric shape factor, σ_e is the effective pressure, P_p is the fluid pressure, and σ_c is the confining stress.

The stress intensity factor has three different modes. The first mode is the tensile mode, or the opening mode, where the two crack surfaces move directly away from each other. The second mode is in-plane shear, or the sliding mode, which occurs when the two crack surfaces move parallel to each other. The third mode is out-of-plane shear, or the tearing mode, which takes place when the crack surfaces slide over each other parallel to the leading edge. The SIFs of the first, second, and third modes are denoted by K_I, K_{II}, and K_{III}, respectively (Farahmand 2012). The first mode is more relevant to our study considering the fractured sample.

For completeness, we define cyclic fracturing here. In cyclic fracturing, the fluid pressure is increased and decreased cyclically until the sample fails. This is different from conventional fracturing, where the fluid pressure is increased monotonically to reach failure in a single cycle. The sample fails when the effective stress intensity factor reaches the fracture toughness (K_{IC}), which is a medium property and does not depend on the loading conditions (Farahmand 2012). The effective stress intensity factor reduces to K_I when only the first mode is active.

Rock failure due to the presence of a crack is governed by the fracture toughness. The rock fails at a lower tensile in cyclic fracturing than in conventional fracturing because the crack length grows with each consecutive cycle. A larger crack length corresponds to a higher SIF for given stress conditions (Eq. 1).

Failure Prediction for Cyclic Loading

Paris law is an empirical relation that predicts the crack growth in cyclic loading (Paris et al. 1961). It allows us to determine the residual life of a sample when its crack size is known. It is valid when the basic assumptions of LEFM are applicable. The crack growth under cyclic loading is predicted as follows (Paris et al. 1961):

$$\frac{da}{dN} = C\Delta K^m \tag{2}$$

where a is the crack length, N is the number of cycles, ΔK is the range in the stress intensity factor at each cycle, and C and m are constants (tuning parameters). The unknown parameters (C and m), which are the solid region properties, are determined by fitting the empirical relation to the lab measurement (Fig. 1).

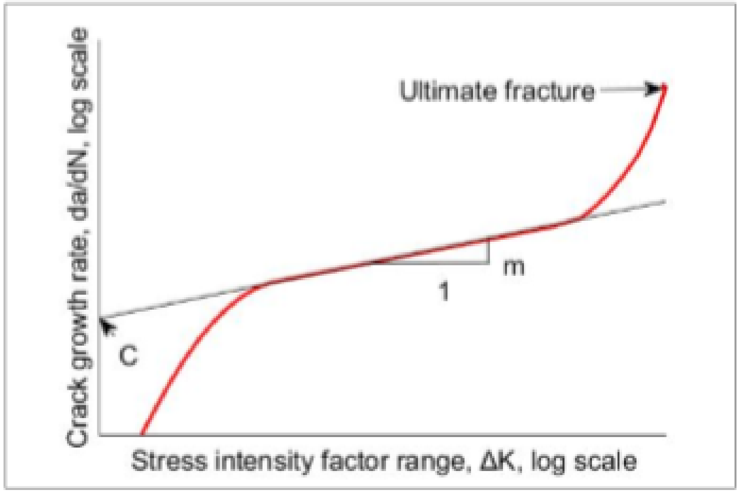

Figure 1: Schematic of crack propagation with change in stress intensity factor in cyclic loading (Paris et al. 1961). Paris law (Eq. 2) is usually applied to the linear (middle) section of the plot.

Paris law is a powerful and yet simple tool. There are more advanced models that require additional lab measurements (Farahmand 2012), which may not be available. Thus, Paris law is very commonly used in fracture mechanics, although its results may be less accurate than the more advanced models.

Cyclic Hydraulic Fracturing of the Sample

We use lab measurements conducted by Patel et al. (2017) in our study, and explain them here for completeness. They cut and polished four cylindrical Tennessee sandstone samples and hydraulically fractured them under triaxial loading conditions. Table 1 lists the pertinent petrophysical properties of the samples.

Table 1: Porosity and permeability of Tennessee sandstone samples (Patel et al. 2017).

Sample	Porosity (%) (500 – 4000 psi)	Permeability (μd) (500 – 4000 psi)
1	4.7 – 4.3	27 - 7
2	5.1 – 4.4	32 - 9
3	4.4 – 3.6	37 - 10
4	5.9 – 6.1	22 - 11

The sample diameter is 4 in and its length is approximately 5.5 in. A hole of ¼ inch in diameter was drilled in the center of the core and extended up to half the sample's length. The hole is completed with a ¼-inch diameter tube that is cemented. We applied triaxial stress (vertical stress = 3000 psi, maximum horizontal stress = 2000 psi, minimum horizontal stress = 500 psi) to replicate the in-situ stress conditions at a 3000 ft depth assuming a 1 psi/ft lithostatic gradient. Figure 2 shows the experimental setup.

Patel et al. (2017) injected oil into the hole at a rate of 10 cm^3/min. First, they fractured two dry samples through conventional loading by increasing the pump pressure monotonically. Then, they fractured the next two via cyclic fracturing where the fluid pressure was increased and decreased cyclically. Table 2 lists the breakdown pressures for the four samples.

Figure 2: Hydraulic fracturing setup (courtesy of Damani et al. 2012). The figure on the left shows an expanded view of the triaxial loading system with axial loading, confining vessel and flat jacks to apply transverse stress. The figure on the right shows the sample covered with copper jacket mounted on the base plate of the triaxial loading system.

Table 2: Breakdown pressures and number cycles for four Tennessee sandstone samples under triaxial loading conditions (vertical stress = 3000 psi, maximum horizontal stress = 2000 psi, minimum horizontal stress = 500 psi). Patel et al. (2017) conducted the lab measurements.

Sample	Fracturing method	Breakdown pressure (psi)	Number of cycles
1	Conventional	2947	1
2	Conventional	3067	1
3	Cyclic	2519	7
4	Cyclic	2900	5

We define a reference breakdown pressure for conventional fracturing as the average breakdown pressures of Samples 1 and 2 (= 3007 psi). Sample 3 had a maximum injection pressure of 300 psi in the first cycle, and Sample 4 had a maximum injection pressure of 1500 psi in the first cycle (Fig. 3). Subsequently, the injection pressure of each cycle was increased by 10% of the reference breakdown pressure in both samples. The minimum pump pressure in each cycle for both samples was 15 psi. The lab measurements show that the breakdown pressure in cyclic fracturing is smaller than in conventional fracturing. The reduction was more pronounced in Sample 2, with a 16% lower value (Patel et al. 2017).

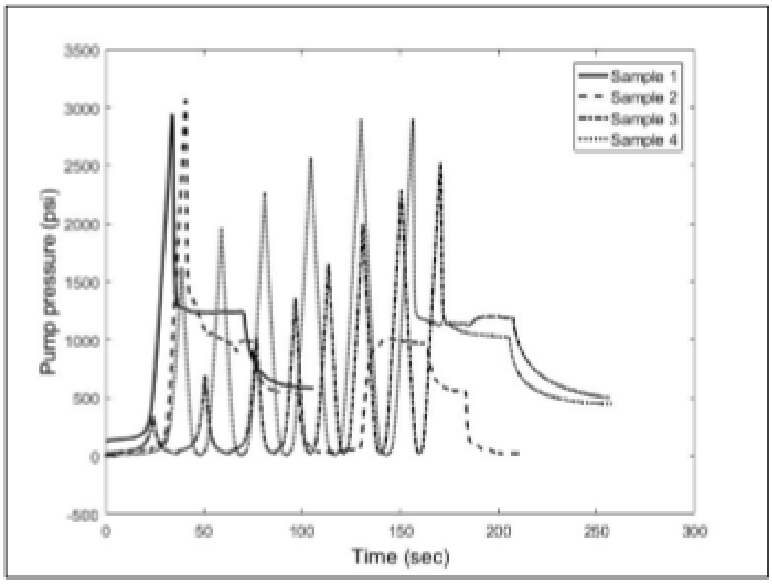

Figure 3: Pump pressure data shows that Samples 1 and 2, which were conventionally fractured, have higher breakdown pressures than the cyclically fractured samples (Patel et al. 2017). The breakdown pressure of Sample 4 is higher than that of Sample 3, but requires fewer cycles to fail.

The rock sample fails at a lower pressure than the conventional breakdown pressure in cyclic fracturing due to the local damage (crack growth) that occurs in each cycle. The small-scale crack propagation in each cycle in consistent with Paris law. Fig. 4 also shows that there are more acoustic events in cyclic fracturing. The increase in the number of acoustic events provides independent evidence for the creation of small-scale cracks.

The higher number of acoustic events in cyclic fracturing indicates that the corresponding stimulated reservoir volume is larger. This is an important advantage of cyclic fracturing compared to conventional fracturing, considering that each acoustic event may be relevant to a small-scale fracture. The higher number of the acoustic events also implies that the effective permeability of the stimulated region increases more significantly than with conventional fracturing.

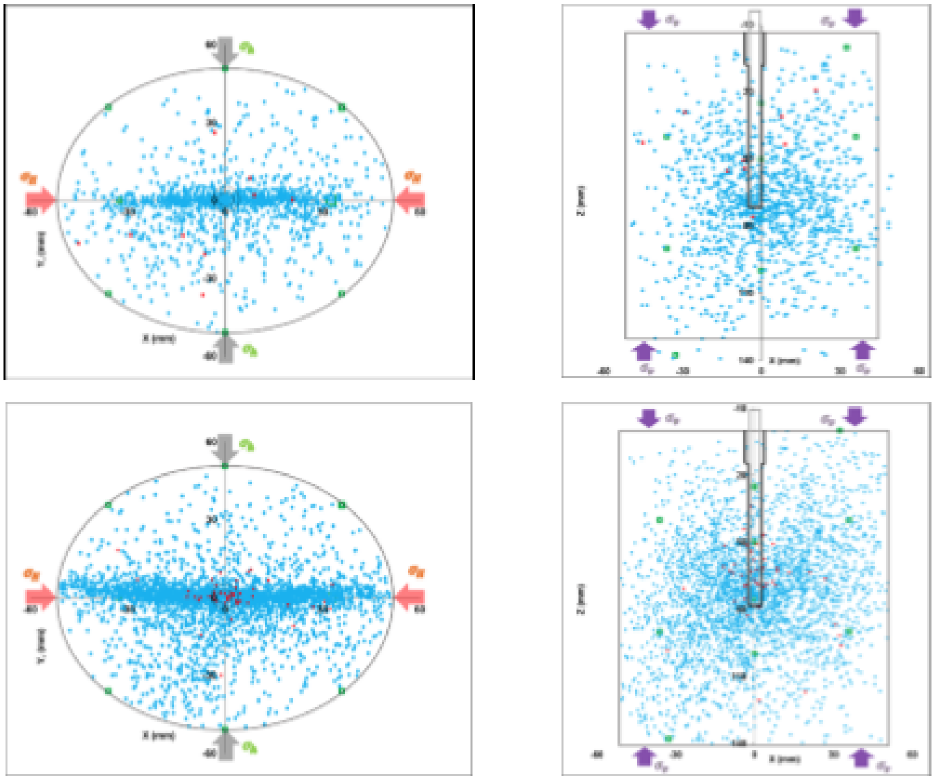

Figure 4: More acoustic events were recorded in cyclic fracturing (bottom) than in the conventional fracturing (top), which suggests that the stimulated reservoir volume and its effective permeability are larger in cyclic fracturing. Patel et al. (2017) conducted the lab measurements under triaxial loading conditions (σ_v (vertical stress) = 3000 psi, σ_H (maximum horizontal stress) = 2000 psi, and σ_h (minimum horizontal stress) = 500 psi).

Methodology

We model cyclic fracturing based on a modified Paris law by accounting for the fracture closure (Elber 1971). Paris law is often used for high-cycle loading or fatigue (HCF), but we apply it to low-cycle fatigue because there is no other model for this range, to the best of our knowledge. The high-cycle loading, or fatigue, is the linear section in Fig. 1. The modified Paris law can be expressed as follows:

$$\frac{da}{dN} = C(U\Delta K)^m \qquad U = 0.5 + 0.4R \qquad R = \frac{K_{min}}{K_{max}} \tag{3}$$

where a is the crack length, N is the number of cycles, ΔK is the change in the stress intensity factor, C and m are constants, U is the Elber constant, and R is the loading ratio.

The modified Paris law has three unknowns (C, m, and initial crack length a_i). The typical range of m is from 0.01 to 30 and of C is from (10^{-1} to 10^{-25}) $\frac{m}{[m\sqrt{Mpa}]^m}$. The initial crack length varies from 0.01 mm to 0.2 mm. We use the corresponding range for each parameter to tune our model. We use the following workflow to determine the unknown parameters in the modified Paris law:

1. The fracture toughness of Tennessee sandstone (K_{IC}) is assigned based on the data available in the literature (Atkinson 1979).
2. The highest effective stress in each cycle is determined by considering the fluid pressure and the confining stress (Sample 3 in our study).
3. The acceptable ranges are established for the unknown parameters (C, m, and a_i).
4. The modified Paris law (Eq. 3) is applied to determine the effective stress intensity factor at the breakdown cycle (K_b). The effective stress intensity factor in our study is equal to K_I.
5. The combinations of the unknown parameters (C, m, and a_i) are changed such that K_b becomes equal to K_{IC}. This step provides the tuned parameters.
6. The tuned parameters are used to predict the stress intensity factor for a given cyclic loading based on the modified Paris law for other samples (Sample 4 in our study).
7. The stress intensity factor based on the tuned parameters at the breakdown pressure (K_b) is compared with the fracture toughness. The corresponding error is calculated as follows:

$$\text{Error } (\%) = \left| \frac{K_b - K_{IC}}{K_{IC}} \right| \times 100 \tag{4}$$

Results

We use the modified Paris law to predict the breakdown pressure for Tennessee sandstone samples. The unknown parameters (C, m, and a_i) are determined based on the workflow provided in the methodology. These coefficients are determined for Sample 3, which is cyclically fractured. There is no unique solution for each unknown parameter and it can have a range of values.

We then use the tuned model, which is the modified Paris law with known coefficients, to predict the breakdown pressure for the last sample (Sample 4). For this, we determine the error associated with using the tuned model (Eq. 4). The fluid pressure at each cycle and the number of cycles for Sample 4 are different from those of Sample 3. Fig. 5 shows that the error associated with using the tuned model for the last sample is smaller than or equal to 15%. The results are promising, but more measurements are required to test the accuracy of the tuned model.

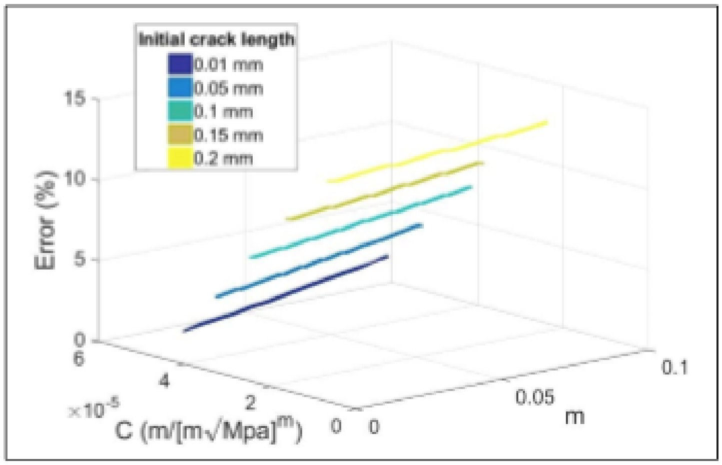

Figure 5: Error (Eq. 4) in predicting the breakdown pressure for cyclic fracturing for Sample 4. The unknown parameters in the modified Paris law are determined based on the workflow provided in the Methodology for Sample 3.

The tuned model allows us to predict the breakdown pressure for different scenarios. Both the fluid pressure and the number of cycles can vary. The tuned model has to be used as an outline in the workflow, and the failure takes place when the difference between the predicted stress intensity factor and the fracture toughness becomes negligible. We consider two cases by changing the fluid pressure cyclically. The first is an example where the fluid pressure is increased at 400-psi increments, and the second is one where the fluid pressure increment is equal to 200 psi. Fig. 6 shows the predicted results, where the sample with smaller pressure increments fails at a lower pressure but at a larger number of cycles.

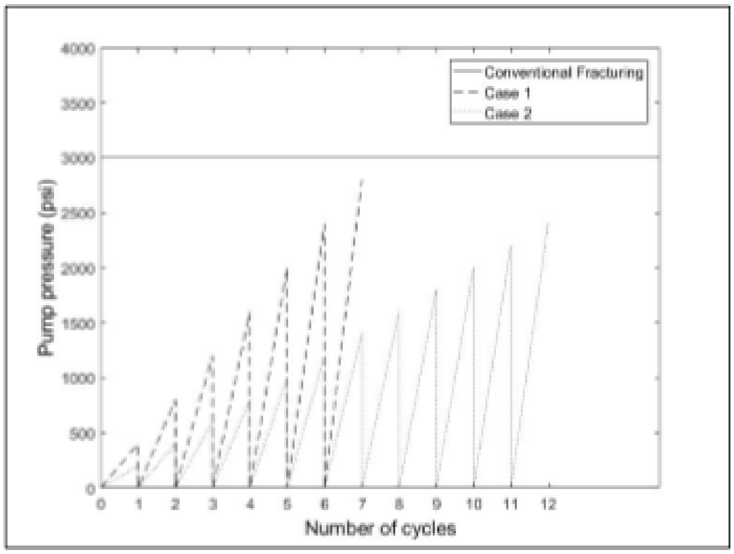

Figure 6: Predicted failure for two hypothetical cases based on the tuned model: Case 1 shows a higher breakdown pressure at a lower number of cycles compared to Case 2.

The tuned Paris law can help us determine the number of cycles and the breakdown pressure. The cyclic fracturing has both positive and negative effects. The number of acoustic events increases in cyclic fracturing (Fig. 4), which corresponds to a larger stimulated reservoir volume and a more significant enhancement in the permeability. The cyclic fracturing also requires more energy and fluid than conventional fracturing, which is a negative effect. This implies that there might be an optimum scenario where the permeability enhancement based on the cyclic fracturing is superior to existing re-stimulation techniques such as re-fracturing. The accurate characterization of the optimum scenario requires more lab measurements to determine the accuracy of the developed model, which is beyond the scope of the present study.

Conclusions

The main objective of the present study was to predict rock failure under cyclic fracturing. We used a modified Paris law, which is based on linear elastic fracture mechanics (LEFM). We determined the unknown parameters of the model based on lab measurements. The tuned model predicted the breakdown pressure of another sample within less than a 15% error. The pump pressures and the number of cycles for the last sample were different from those of the sample used for tuning purposes. The modified Paris law was adopted here in petroleum engineering for the first time, although it is widely used for fatigue life prediction in mechanical and aerospace engineering. Cyclic fracturing has the potential to be used as a new stimulation technique, especially if its outcome can be accurately predicted. The results of the modified Paris law are promising, but more measurements are required to fully test its accuracy.

Acknowledgements

The authors are grateful for the lab measurements (Patel et al. 2017) shared by the Unconventional Shale Gas Consortium at The University of Oklahoma.

Nomenclature

a = crack length
a_i = initial crack length
C = Paris law constant
HCF = high-cycle fatigue
K = stress intensity factor
K_I = mode I stress intensity factor
K_{IC} = fracture toughness
K_{II} = mode II stress intensity factor
K_{III} = mode III stress intensity factor
K_b = stress intensity factor at the breakdown cycle
K_{max} = maximum stress intensity factor
K_{min} = minimum stress intensity factor
K_{th} = threshold stress intensity factor
LCF = low-cycle fatigue
LEFM = linear elastic fracture mechanics
M = Paris law constant
N = number of cycles in cyclic fracturing
P_p = pore pressure
R = load ratio
SIF = stress intensity factor
U = Elber's constant
Y = geometric shape factor
σ_c = confining stress
σ_e = effective stress
σ_h = minimum horizontal stress
σ_H = maximum horizontal stress
σ_v = vertical stress

References

1. Atkinson, B. K. 1979, February. Fracture toughness of Tennessee sandstone and Carrara marble using the double torsion testing method. In International Journal of Rock Mechanics and Mining Sciences & Geomechanics Abstracts, 16(1), 49−53.

2. Damani, A., Sharma, A., Sondergeld, C. et al. 2012. Acoustic emission and SEM analyses of hydraulic fractures under triaxial stress conditions. In SEG Technical Program Expanded Abstracts 2012, 1−5. Society of Exploration Geophysicists.

3. Donahue, R. J., Clark, H. M., Atanmo, P. et al. 1972. Crack opening displacement and the rate of fatigue crack growth. International Journal of Fracture, 8(2), 209−219.

4. Elber, W. 1971. The significance of fatigue crack closure. In Damage tolerance in aircraft structures. ASTM International.

5. Erdogan, F., and Ratwani, M. 1970. Fatigue and fracture of cylindrical shells containing a circumferential crack. International Journal of Fracture Mechanics, 6(4), 379−392.

6. Farahmand, B. 2012. Fracture mechanics of metals, composites, welds, and bolted joints: application of LEFM, EPFM, and FMDM theory. Boston: Kluwer Academic Publishers.

7. Forman, R. G., Keamey, V. E., and Engle, R. M. 1967. Numerical analysis of crack propagation in a cyclic-loaded structure. J. Basic Engineering. Trans ASME, 89, 459−464.

8. Griffith, A. A. 1920. The phenomena of flow and rupture in solids: Phil. Trans. Roy. Soc. Lond. Ser. A, 221, 163−98.

9. Inglis, C. E. 1913. Stresses in a plate due to the presence of cracks and sharp corners. Trans Naval Architect, 55, 219−242.

10. Irwin, G. R. 1957. Analysis of stresses and strains near the end of a crack traversing a plate. Journal of Applied Mechanics. Vol. 24, 361−364.

11. Paris, P. C., Gomez, M. P., and Anderson, W. E. 1961. A rational analytic theory of fatigue. The trend in engineering, 13(1), 9−14.

12. Patel, S. M., Sondergeld, C. H., and Rai, C. S. 2017. Laboratory studies of hydraulic fracturing by cyclic injection. International Journal of Rock Mechanics and Mining Sciences, 95, 8−15.

13. Sakhaee-Pour, A., Gowhari-Anaraki, A. R., and Hardy, S. J. 2010. The effect of stiffness on stress intensity factor for a crack in annular disc under constant central torque. International Journal of Damage Mechanics, 19(8), 1001−1015.

14. Shigley, J. E., Mischke, C. R., and Budynas, R. G. 2004. Mechanical engineering design. New York: McGraw-Hill.

15. Stephens, R. I., Fatemi, A., Stephens, R. R., et al. 2000. Metal fatigue in engineering. New York: John Wiley & Sons.